Multivariate Age-related Analysis of Variance in quantitative MRI maps: Widespread age-related differences revisited.

[1]Soodeh Moallemian, [1]Christine Bastin, [2]Martina F. Callaghan*, [1]Christophe Phillips*

[1]GIGA-Cyclotron Research Centre-in Vivo imaging, University of Liège, Belgium

[2]Wellcome Centre for Human Neuroimaging, UCL Queen Square Institute of Neurology, University College London, UK

* Authors equally contributed.

Abstract

This study utilized multivariate ANOVA analysis to investigate age-related microstructural changes in the brain tissues driven primarily by myelin, iron, and water content. Voxel-wise analyses were performed on gray matter (GM) and white matter (WM), in addition to region of interest (ROI) analyses. The multivariate approach identified brain regions showing coordinated alterations in multiple tissue properties and demonstrated bidirectional correlations between age and all examined modalities in various brain regions, including the caudate nucleus, putamen, insula, cerebellum, lingual gyri, hippocampus, and olfactory bulb. The multivariate model was more sensitive than univariate analyses as evidenced by detecting a larger number of significant voxels within clusters in the supplementary motor area, frontal cortex, hippocampus, amygdala, occipital cortex, and cerebellum bilaterally. The examination of normalized, smoothed, and z-transformed maps within the ROIs revealed age-dependent differences in myelin, iron, and water content. These findings contribute to our understanding of age-related brain differences and provide insights into the underlying mechanisms of aging. The study emphasizes the importance of multivariate analysis for detecting subtle microstructural changes associated with aging that may motivate interventions to mitigate cognitive decline in older adults.

Keywords: quantitative MRI, aging, multivariate model, myelin, iron content, water concentration

1. Introduction

Aging is an inevitable part of our lifecycle that is associated with physical deterioration of different organs. Various hallmarks of aging have been identified over the past years that associate with neurodegenerative pathological changes in the brain, making age a primary risk factor for most neurodegenerative diseases including Alzheimer's disease (AD), Parkinson's disease (PD), and frontotemporal lobar dementia (FTD) [1,2].

Quantitative MR imaging (qMRI) enables us to extract sensitive and specific information about the microstructural properties of the brain tissue in vivo, such as axon, myelin, iron and water concentration [3]. The estimation of (semi-)quantitative metrics normally includes effective transverse relaxation rates (R2*), which is primarily sensitive to iron, longitudinal relaxation rate (R1), which is sensitive to iron, myelin and water content, proton density (PD), indicative of free water content, and magnetization transfer saturation (MTsat), associated with macromolecular content, predominantly myelin [4,5]

Many studies of aging focus on alterations in the nervous system, such as (de-)myelination or iron accumulation [6,7]. Callaghan et al. investigated age-related differences of biologically relevant in vivo measures over the course of normal aging using quantitative multiparameter mapping (MPM) and showed significant demyelination in white matter (WM), concurrent with an increase in iron levels in the basal ganglia, red nucleus, and extensive cortical regions, but decreases along the superior occipitofrontal fascicle and optic radiation [8]. Steiger et al. investigated the difference in iron and myelin levels between two groups of young and older participants using qMRI, and showed that age-related higher levels of iron are accompanied by a negative correlation of iron and myelin in the ventral striatum [9]. Although demyelination primarily affects the WM of the brain, recent research shows that it can also occur in gray matter (GM), which is made up of cell bodies of neurons. Studies have shown that gray matter myelination can occur during development, particularly in the prefrontal cortex, and may continue throughout late adulthood in response to learning and experience [10,11]. Khattar and colleagues assessed the association of myelination and iron accumulation in the aging brain of a cohort of 21-94 year-old healthy

controls and found a negative correlation between whole brain myelin water fraction and iron content in most brain regions; they also highlight that the myelination continues until middle age overall in the brain [12]. [5]. reported robust evidence for spatial overlap between volume, myelination, and iron decomposition changes in aging that affect predominantly motor and executive networks under a modified normal probability curve approach from the Permutation Analysis of Linear Models (PALM) toolbox [13,14].

In this technical note, we re-analyze the data from[8] with a multivariate modeling approach as implemented in MSPM toolbox [15] to assess the advantages of such an approach, in term of sensitivity and specificity, over the conventional multiple univariate analysis.

2. Method

2.1. Participants and data preprocessing

We took advantage of the processed data from [8], which include 138 healthy participants aged 19-75 years (35.5% male, mean = 46.64, s.d = 21). Quantitative multiparameter maps (R1, R2*, PD, and MTsat) were reconstructed with the VBQ toolbox, a preliminary version of the hMRI toolbox [16,17]. Processing steps included segmentation and diffeomorphic morphing to MNI space using DARTEL [18]. Tissue-weighted smoothing (for GM and WM separately) with a 3mm FHWM isotropic kernel applied to account for residual misalignment while preserving the quantitative nature of the data. Finally, group level GM and WM masks were created to be further used as exclusive masks in the statistical analysis. For full details see [8].

2.2. Univariate GLM analyses

In this re-analysis, the 8 resulting sets of qMRI maps were z-transformed per modality and across subjects to ensure comparability between maps utilizing the mean and variance over each voxel. This procedure ensured comparability of different modalities for our multivariate analysis. The univariate general linear models were performed on each map (after z-transformation) using age, gender, total intracranial volume (TIV), and scanner as regressors. To assess the correlation

between the individual tissue property maps and age, an F-test was performed on each map at voxel-level over GM and WM separately. All univariate statistical analyses were performed under the general linear model framework in SPM12, considering two p-value, .05 and .0125, family wise error rate corrected (FWER) thresholds. The latter threshold accounts for the fact that for both tissue classes, 4 similar inferences are performed (one per map) thus applying a Bonferroni correction the applied threshold is divided by 4, i.e., .0125= .05/4.

2.3. Multivariate GLM (mGLM)

The multivariate GLM (mGLM) is specified using the design matrices of the 4 univariate models in the MSPM toolbox [15]. The mGLM models the multivariate observations at each voxel as $Y = XB + E$, where $Y_{138\times4} = [Y_1, Y_2, Y_3, Y_4]$ is the multi-modal data matrix, each row of Y represents one participant, and each column represents one map; and $X_{138\times5} = [X_1, X_2, X_3, X_4, X_5]$ is the design matrix, the first column represents the mean over subjects, the rest of the columns represent mean-centered regressors (age, TIV, gender, scanner) respectively. Thus, B is a 5×4 matrix of regression coefficients; and E is the residual matrix of size 138×4. B is estimated using an ordinary least-square method, as $\hat{B} = (X^T X)^{-1} X^T X$. The residual matrix $\hat{E}$ is estimated on a per-voxel basis that allows for a straightforward determination of a unique covariance structure for each voxel. This feature is a significant advantage of mass multivariate approaches when dealing with dependent neuroimaging data. However, it is important to note that in this framework, the assumption of normality for the residuals implies that the covariance structure is assumed to be the same across different groups or conditions. There is an assumed degree of correlation between the columns of Y, this correlation is expressed by estimation of variance-covariance matrix $\hat{\Sigma} = \frac{1}{n-k} \hat{E}^{\mathrm{T}} \hat{E}$, where n is the number of subjects and k is number of covariates.

Hypothesis testing

Hypothesis testing in mGLM, relies on testing the linear contrast $CBL = 0$. This extension of the univariate scheme combines standard hypotheses on the rows of matrix B, represented by matrix C, with hypotheses on the columns of B, represented by matrix L. In the context of multivariate ANOVA (MANOVA) models, contrasts of main effects and interactions are formulated by setting $L = I_t$, the $t \times t$ identity matrix, as the dependent variables in multimodal neuroimaging applications are not assumed to be directly proportional. This method is the most suitable for conducting hypothesis testing on multimodal neuroimaging applications.

Test statistics in mGLM

In hypothesis testing using the multivariate GLM, there are four standard test statistics available, which can be constructed based on the calculation of two sums-of-squares and cross-products (SSCP) matrices: Pillai's trace [19], Wilks' lambda [20], Hotelling-Lawley trace [21], and Roy's largest root [22]. For any particular contrast, there is an SSCP matrix associated with the hypothesis.

$$SSCP_{hypo} = \left(C\hat{B}L^T\right)^T (C(X^TX)^{-1}C^T)(C\hat{B}L^T) \quad (1)$$

And an SSCP matrix associated with the residuals.

$$SSCP_{residual} = L\left(\hat{E}^T E\right)L^T \quad (2)$$

These matrices are generalizations of the numerator and denominator sums-of-squares from the univariate GLM hypothesis-testing approach. When L is an identity matrix, the main diagonal of $SSCP_{hyppo}$ contains the sums of squares for the hypothesis in C as applied to the estimated parameters for each dependent variable separately. And $SSCP_{residual}$ matrix is an unscaled form of the estimated covariance matrix $\hat{\Sigma}$.

Construction of the test statistics rely on some linear combination of m eigenvalues $(\lambda_1, \ldots, \lambda_q)$ of $SSCP_{residual}^{-1} SSCP_{hyppo}$. Here, we will only focus on Wilks' lambda test statistics. It

quantifies the proportion of variance not accounted for by the hypothesis compared to the total variance in the data.

The Wilks Lambda statistic can be calculated based on the calculated m eigenvalues as $\Lambda = \prod_{i=1}^{m} \frac{1}{1+\lambda_i}$. This has an approximate F distribution with degrees of freedoms a and b:

$$F(a,b) = \frac{1-\Lambda^{\frac{1}{t}}}{\Lambda^{\frac{1}{t}}} \cdot \frac{b}{a} \tag{3}$$

Where $a = lq$ and $b = rt - 2u$.

$$l = rank(Y) \tag{4}$$

$$q = rank(X) \tag{5}$$

$$u = \frac{a-2}{4} \tag{6}$$

$r = N - q - \frac{a+1}{2}$, N = sample size (7)

$$t = \begin{cases} \sqrt{\frac{l^2q^2-4}{l^2+q^2-5}} & , l^2+q^2-5 > 0 \\ 1 & , l^2+q^2-5 \leq 0 \end{cases} \tag{8}$$

If the minimum value between $l = 4$ and $q = 1$ is ≤ 2, the distribution is exactly F.

Age related microstructural changes- mGLM

The hypothesis $H_0: CBL = 0$ can be tested to assess the different potential co-occurrence of change between the modalities. To test the joint effect on the 4 quantitative maps in a specific tissue type, $L_{4\times4}$ is defined as an identity matrix corresponding to the number of dependent variables (quantitative maps). As explained before, each column of L will perform a univariate analysis on each column of B. Here, C was defined as $[0\ 1\ 0\ 0\ 0]$ to only see the correlation between age and maps. In this case, Λ has an exact F distribution with a = 4 and b = 130 degrees of freedom.

Canonical Correlation Analysis

Canonical vectors are calculated under the assumption that matrix L involves multiple dependent variables ($l > 1$), to extract the contribution of each dependent variable to the test statistics Λ. This contribution corresponds to the eigen vectors of the eigen decomposition of $SSCP_{residuals}^{-1} SSCP_{hyppo}$. [23].

2.4. ROI analyses

The age-related parameter differences in selected regions, including caudate, cerebellum, hippocampus, middle frontal gyrus, pallidum, putamen, superior motor cortex, heschl and precentral gyri, and thalamus, will be further described. ROIs were defined according to the Neuro-morphometrics, Inc[24] and selected based on identified significant areas in our mGLM results and in [8]. For each participant and quantitative map, the measure from each voxel in an ROI was extracted. The regressors of no interest (gender, TIV and scanner) were regressed out, and for each selected ROI, the relation between age and median value across subjects will be examined post hoc.

3. Results

The analyses were conducted on both gray matter (GM) and white matter (WM). Consequently, explicit non overlapping masks for GM and WM were applied to each analysis. Since each parametric map has its specific unit, such as Hertz for R2* images and p.u. for MTsat maps, their values cannot be directly compared. All statistical analyses were performed on standardized z-transformed data. The multivariate statistical analyses were conducted at a corrected threshold of p<.05 FWER. The univariate analyses were thresholded twice: once at p<.05 FWER corrected to replicate the results from a previously published paper [8], and once at p<.0125 FWER corrected to account for the effect of multiple comparisons.

3.1. uGLM vs mGLM: Voxel level analyses

The individual GM and WM analyses on R2*, PD, MTsat, and R1 maps at a corrected threshold of p<.05 FWER, concur with those in [8]. The statistical parametric maps for age-related changes in the microstructure of the brain in GM and WM (at a corrected threshold of p<.05 FWER) are depicted in Figure sup-1 and Figure sup-2 of the supplementary data. The statistical parametric maps for the same analyses at a corrected threshold of p<.0125 FWER) are presented in Figure 1 and 2 for GM and WM respectively.

Voxel-wise mGLM results presented in Figure 3, indicate bidirectional correlation between all modalities and age at p<.05 FWER corrected. The correlation is observed bilaterally in caudate nucleus, putamen, insula, cerebellum, lingual gyri, hippocampus, and olfactory bulb.

Table 1 provides a statistical summary of the F-tests results (thresholded at voxel-level p<.05 FWER) from both the univariate general linear models (uGLMs) and mGLM for all maps within the two tissue classes. Additionally, Table 2 presents the statistical summary of the uGLM F-tests results with Bonferroni-adjusted threshold. Comparing the spatial extent of significant results between uGLMs and mGLM in Tables 1 and 2 reveals that the multivariate model identifies a larger number of significant voxels compared to the union of all uGLMs with both family-wise error (FWE) and Bonferroni corrections.

To illustrate the voxels affected by age at a threshold of p<.0125 and p<.05 in at least one of the (semi-)quantitative maps, the union of all statistical parametric maps derived from uGLMs in GM was binarized and depicted in panels A and B of Figure 4.

In Figure 5, the differentiates of the binarized union of all statistical parametric maps derived from the uGLMs (with p<.0125 FWER) in GM and the binarized statistical parametric map for

mGLM (with p<.05 FWER) to visualize the voxels that can be uniquely detected either by the multivariate model (shown in red) or by at least one of the univariate models (shown in green). Among the models used, only the mGLM detected an age effect in certain regions, including portions of the superior medial frontal lobe, supplementary motor area, paracentral lobule, middle and anterior cingulum, parts of the precuneus, cuneus, calcarine, lingual gyrus, cerebellum, hippocampus, and para hippocampus bilaterally, as well as the left fusiform gyrus. Schematic representations of these regions can be found in Figure 5, highlighted in red.

3.2. ROI analyses

Canonical vectors

To further investigate the impact of aging on myelination, iron content, and water concentration in various brain regions, quantitative MR parameters were selected from bilateral regions including the putamen, thalamus, hippocampus, cerebellum, caudate, middle frontal gyrus, precentral gyrus, heschl gyrus, supplementary motor area, caudate, and pallidum [7,8,25,26].

For each region of interest (ROI), the canonical vectors corresponding to each quantitative map within the gray matter (GM) were estimated, as shown in the upper panel of Figure 6. It is important to note that the canonical vectors displayed in the lower part of Figure 6 represent the contribution of each map in the peak voxel of the respective ROI and do not represent the contribution factor for the entire ROI. Additionally, the direction of these vectors cannot be interpreted as they are derived from F-tests, therefore we have displayed the absolute weights. For example, in the right and left hippocampus, PD signals exhibit the highest contribution while in the right putamen, MTsat signal contributes the most as indicated by the canonical vectors.

Median values

The median values of normalized, smoothed, and z-transformed R2*, MTsat, PD, and R1 maps within the Putamen and Hippocampus ROIs with respect to age are illustrated in Figures 7 and 8. Region-based regression analysis for the adjusted medians and age, within each cluster are along with the respective linear age dependence observed from the uGLM analyses in the selected regions.

We observe a bilateral decrease in the normalized MTsat and PD values in GM with respect to aging. While the PD and MTsat median values decrease with age in all regions of the brain, median R2* values show an increase in most regions of the brain except for the thalamus where there is a significant negative age related variation. These results are consistent with previously published results for the mean values in thalamus for R2* [5]. R1 median signals show a weak positive correlation with age. The alteration in median values as a function of age concurs with the magnitude of the associated canonical vector. The bivariate correlation analysis indicates strongest correlations for PD in most selected regions, see Table 3.

4. Discussion:

The multivariate approach used in this study to investigate age-related changes in the microstructural tissue properties of the brain, incorporating image-derived quantitative maps for myelin, iron, and free water content, enables the identification of regions that are influenced by the simultaneous occurrence of various parameter differences.

By considering multiple quantitative maps simultaneously, the multivariate approach provides a comprehensive understanding of how these different tissue properties interact and contribute to age-related differences. This method enables the identification of specific brain regions that exhibit coordinated alterations in myelin, iron, and water content, offering insights into the underlying mechanisms of aging.

The observed differences in the quantitative MR parameters align with findings from *ex vivo* histologic studies and demonstrate a high specificity for tissue properties, including myelin content, iron content, and free water content.

Using voxel-wise analysis with the multivariate GLM (mGLM), a bidirectional correlation between age and all the examined modalities was observed bilaterally in various brain regions. These regions encompassed the caudate nucleus, putamen, insula, cerebellum, lingual gyri, hippocampus, and olfactory bulb. Importantly, the multivariate approach demonstrated advantages over univariate analyses that focus on individual tissue parameters separately.

While examining individual tissue properties in isolation may provide insights into specific aspects of brain aging, the multivariate model revealed large clusters in the brain that could not be detected by analyzing each property individually. This indicates that the combined examination of multiple tissue properties enables the detection of additional regions associated with aging despite the presence of contrary changes in different properties. As observed in Table 2, mGLM outperformed the individual univariate GLMs (uGLMs) by detecting a larger number of significant voxels within clusters that cover the supplementary motor area, frontal cortex, hippocampus, amygdala, occipital cortex, and cerebellum bilaterally. This finding suggests that mGLM is a more effective/sensitive technique for detecting age-related differences in the brain.

In this study, the application of a multivariate model such as MANOVA proves advantageous due to the well-established correlations among brain tissue characteristics and the interrelated nature of quantitative map values. By accounting for this inherent correlation, MANOVA effectively reduces potential biases in the results that could arise from using multiple ANOVAs. MANOVA's ability to consider the complex relationships between multiple variables allows it to

detect effects that might be smaller than those detectable by ANOVA, providing a more comprehensive understanding of the data.

Additionally, independent covariates can affect the relationship between the brain microstructure characteristics rather than influencing only a single variable; such patterns cannot be detected by the univariate models. Moreover, MANOVA offers a convenient means to manage the family-wise error rate when simultaneously analyzing multiple dependent variables, effectively reducing type-1 errors. In this study, where four different variables were examined concurrently, better results were achieved under the same p-value threshold compared to multiple univariate analyses on the same GM and WM maps. This underscores the robustness and appropriateness of a multivariate approach for understanding the intricate relationships within the dataset. Here, we utilized Bonferroni threshold for combining the p-values to build up the same power for univariate and multivariate techniques. However, there are other methods for combining p-values for detection of partial association such ad Fisher and weighted Fisher methods, which are more relevant in case of many comparisons [27].

The nonlinear relationship between MTsat values and age, as visible in Figures 6 and 7, could be explained by the fact that myelination is not limited to early development, but can also occur throughout adulthood, with the pattern of myelination depending on the hierarchy of connections between different brain regions [6,11,28]. Potential nonlinear age dependency is also seen in the R2* profile in some regions such as amygdala and putamen (Figure 7) which could be due to slower accumulation of iron in these regions. Hagiwara et al. showed the nonlinear behavior of different brain tissue properties [29]. However, within the scope of this study, we limited our examination to linear age-related variations, as in the original analysis of these data.

The canonical vectors shown in Figure 6, indicate the contribution of each modality in the multivariate model at the peak voxels in the selected ROIs. Of note, the canonical vectors can only highlight the contribution by their size and cannot inform us about the direction of the effect.

The ROI-based partial Pierson's correlations, presented in Table 3, are evidence of stronger correlations between the GM PD maps and age, which concur with the canonical weights regarding the contribution of PD maps within the GM.

Limitations and conclusion

It is important to note that MANOVA differs from multiple ANOVA analyses, as it does not focus on the signal-to-noise ratio of independent variable effects on each dependent variable individually. Instead, it tests for effects of interest on a combination of outcome variables. For an assessment of the former, a return to univariate analyses is necessary.

Aging involves not only microstructural changes in the brain but also macrostructural and functional alterations, such as changes in GM and WM volume and cognitive behavior changes. Therefore, there remains a need to investigate aging by considering different combinations of changes together. Furthermore, longitudinal studies are required to elucidate how normal aging deviates from pathological aging within a multivariate system.

In summary, the findings of this study underscore the importance of employing advanced statistical models like the mGLM to detect subtle microstructural changes associated with aging. The results highlight the significance of ROI analyses in identifying specific brain regions affected by aging and their relationships with different modalities. This study provides valuable insights into the neural mechanisms underlying age-related differences in brain structure, which

may have implications for developing effective interventions to slow down or prevent cognitive decline in older adults.

Data Availability

The processed data used in this study will be available in…

Acknowledgments

The authors would like to thank E. Anderson, M. Cappelletti, R. Chowdhury, J. Diedirchsen, T.H.B. Fitzgerald and P. Smittenaar who took part in data acquisition as part of multiple cognitive neuroimaging studies performed at the WCHN.

Funding

This work was supported by the Walloon Region in the framework of the PIT program PROTHER-WAL under grant agreement No. 7289. CB and CP are respectively Senior Research Associate and Research Director at the F.R.S.-FNRS.

Disclosure statement

The authors declare that this research was conducted in the absence of any commercial or financial relationships that could be construed as a potential conflict of interest.

Supplementary

Figure sup-1, Figure sup-2, Table sup-1.

References:

1. Azam S, Haque ME, Balakrishnan R, Kim IS, Choi DK. The Ageing Brain: Molecular and Cellular Basis of Neurodegeneration. *Front Cell Dev Biol*. 2021;9:683459. doi:10.3389/fcell.2021.683459

2. Jeremic D, Jiménez-Díaz L, Navarro-López JD. Past, present and future of therapeutic strategies against amyloid-β peptides in Alzheimer's disease: a systematic review. *Ageing Res Rev*. 2021;72:101496. doi:10.1016/j.arr.2021.101496

3. Weiskopf N, Edwards LJ, Helms G, Mohammadi S, Kirilina E. Quantitative magnetic resonance imaging of brain anatomy and in vivo histology. *Nat Rev Phys*. 2021;3(8):570-588. doi:10.1038/s42254-021-00326-1

4. Tabelow K, Balteau E, Ashburner J, et al. hMRI – A toolbox for quantitative MRI in neuroscience and clinical research. *NeuroImage*. 2019;194:191-210. doi:10.1016/j.neuroimage.2019.01.029

5. Taubert M, Roggenhofer E, Melie-Garcia L, et al. Converging patterns of aging-associated brain volume loss and tissue microstructure differences. *Neurobiol Aging*. 2020;88:108-118. doi:10.1016/j.neurobiolaging.2020.01.006

6. Peters A. The effects of normal aging on myelin and nerve fibers: A review. *J Neurocytol*. Published online 2002:13.

7. Tian Y, Tian Y, Yuan Z, et al. Iron Metabolism in Aging and Age-Related Diseases. *Int J Mol Sci*. 2022;23(7):3612. doi:10.3390/ijms23073612

8. Callaghan MF, Freund P, Draganski B, et al. Widespread age-related differences in the human brain microstructure revealed by quantitative magnetic resonance imaging. *Neurobiol Aging*. 2014;35(8):1862-1872. doi:10.1016/j.neurobiolaging.2014.02.008

9. Steiger TK, Weiskopf N, Bunzeck N. Iron Level and Myelin Content in the Ventral Striatum Predict Memory Performance in the Aging Brain. *J Neurosci*. 2016;36(12):3552-3558. doi:10.1523/JNEUROSCI.3617-15.2016

10. Fields RD. White matter in learning, cognition and psychiatric disorders. *Trends Neurosci*. 2008;31(7):361-370. doi:10.1016/j.tins.2008.04.001

11. Timmler S, Simons M. Grey matter myelination. *Glia*. 2019;67(11):2063-2070. doi:10.1002/glia.23614

12. Khattar N, Triebswetter C, Kiely M, et al. Investigation of the association between cerebral iron content and myelin content in normative aging using quantitative magnetic resonance neuroimaging. *NeuroImage*. 2021;239:118267. doi:10.1016/j.neuroimage.2021.118267

13. Winkler AM, Webster MA, Brooks JC, Tracey I, Smith SM, Nichols TE. Non-parametric combination and related permutation tests for neuroimaging. *Hum Brain Mapp*. 2016;37(4):1486-1511. doi:10.1002/hbm.23115

14. Winkler AM, Ridgway GR, Webster MA, Smith SM, Nichols TE. Permutation inference for the general linear model. *NeuroImage*. 2014;92:381-397. doi:10.1016/j.neuroimage.2014.01.060

15. Gyger L, Ramponi C, Mall JF, et al. Temporal trajectory of brain tissue property changes induced by electroconvulsive therapy. *NeuroImage*. 2021;232:117895. doi:10.1016/j.neuroimage.2021.117895

16. Draganski B, Ashburner J, Hutton C, et al. Regional specificity of MRI contrast parameter changes in normal ageing revealed by voxel-based quantification (VBQ). *NeuroImage*. 2011;55(4):1423-1434. doi:10.1016/j.neuroimage.2011.01.052

17. Tabelow K, Balteau E, Ashburner J, et al. hMRI – A toolbox for quantitative MRI in neuroscience and clinical research. *Neuroimage*. 2019;194:191-210. doi:10.1016/j.neuroimage.2019.01.029

18. Ashburner J. A fast diffeomorphic image registration algorithm. *NeuroImage*. 2007;38(1):95-113. doi:10.1016/j.neuroimage.2007.07.007

19. Pillai KCS. Some New Test Criteria in Multivariate Analysis. *Ann Math Stat*. 1955;26(1):117-121. doi:10.1214/aoms/1177728599

20. Wilks SS. Certain Generalizations in the Analysis of Variance. *Biometrika*. 1932;24(3/4):471-494. doi:10.2307/2331979

21. Hotelling H. A generalized T test and measure of multivariate dispersion. *Proc Second Berkeley Symp Math Stat Probab*. Published online 1951:23-41.

22. Roy SN. The Individual Sampling Distribution of the Maximum, the Minimum and Any Intermediate of the p-Statistics on the Null-Hypothesis on JSTOR. *Indian J Stat 1933-1960*. 1945;7(2):133-158.

23. Tabachnick BG, Fidell LS. *Using Multivariate Statistics*. 5th ed. Pearson/Allyn & Bacon; 2007.

24. Bakker R, Tiesinga P, Kötter R. The Scalable Brain Atlas: Instant Web-Based Access to Public Brain Atlases and Related Content. *Neuroinformatics*. 2015;13(3):353-366. doi:10.1007/s12021-014-9258-x

25. Darnai G, Nagy SA, Horváth R, et al. Iron Concentration in Deep Gray Matter Structures is Associated with Worse Visual Memory Performance in Healthy Young Adults. *J Alzheimers Dis*. 2017;59(2):675-681. doi:10.3233/JAD-170118

26. Wang F, Ren SY, Chen JF, et al. Myelin degeneration and diminished myelin renewal contribute to age-related deficits in memory. *Nat Neurosci*. 2020;23(4):481-486. doi:10.1038/s41593-020-0588-8

27. Yoon S, Baik B, Park T, Nam D. Powerful p-value combination methods to detect incomplete association. *Sci Rep*. 2021;11(1):6980. doi:10.1038/s41598-021-86465-y

28. Snaidero N, Simons M. Myelination at a glance. *J Cell Sci*. 2014;127(Pt 14):2999-3004. doi:10.1242/jcs.151043

29. Hagiwara A, Fujimoto K, Kamagata K, et al. Age-Related Changes in Relaxation Times, Proton Density, Myelin, and Tissue Volumes in Adult Brain Analyzed by 2-Dimensional Quantitative Synthetic Magnetic Resonance Imaging. *Invest Radiol*. 2021;56(3):163-172. doi:10.1097/RLI.0000000000000720

List of Figures:

List of Tables:

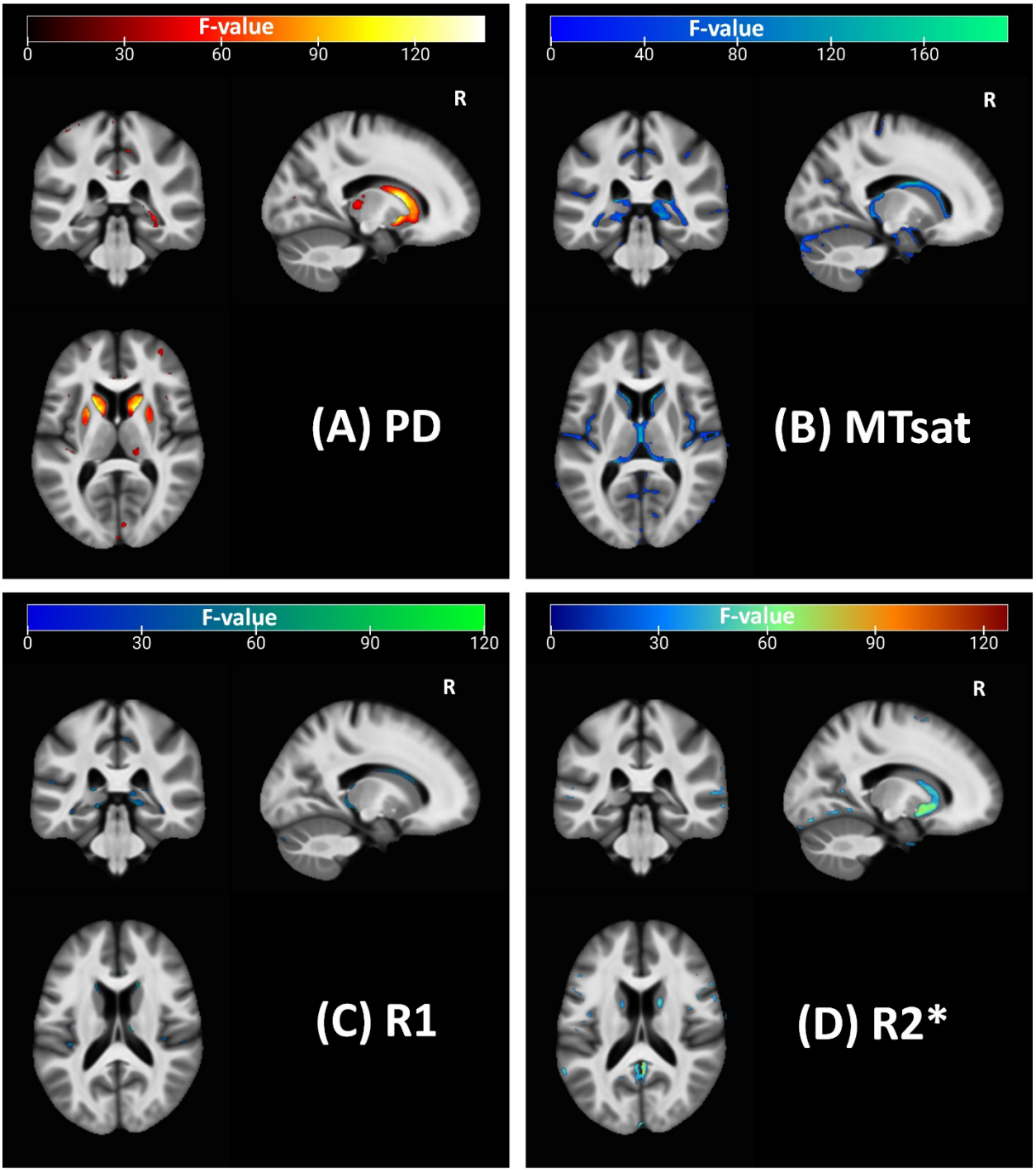

Figure 1. Statistical parametric maps of uGLMs in GM*; showing all the voxels with significant correlation with age, as detected by uGLMs for PD, MTsat, R1, and R2* maps. The F-tests were thresholded at p<0.0125 FWER corrected at voxel-level. The SPMs were overlayed on the mean MTsat map for the cohort in the MNI space. Abbreviation: GLM, general linear model; uGLM, univariate GLM; GM, gray matter; FWER, family-wise error rate; SPM, statistical parametric map.*

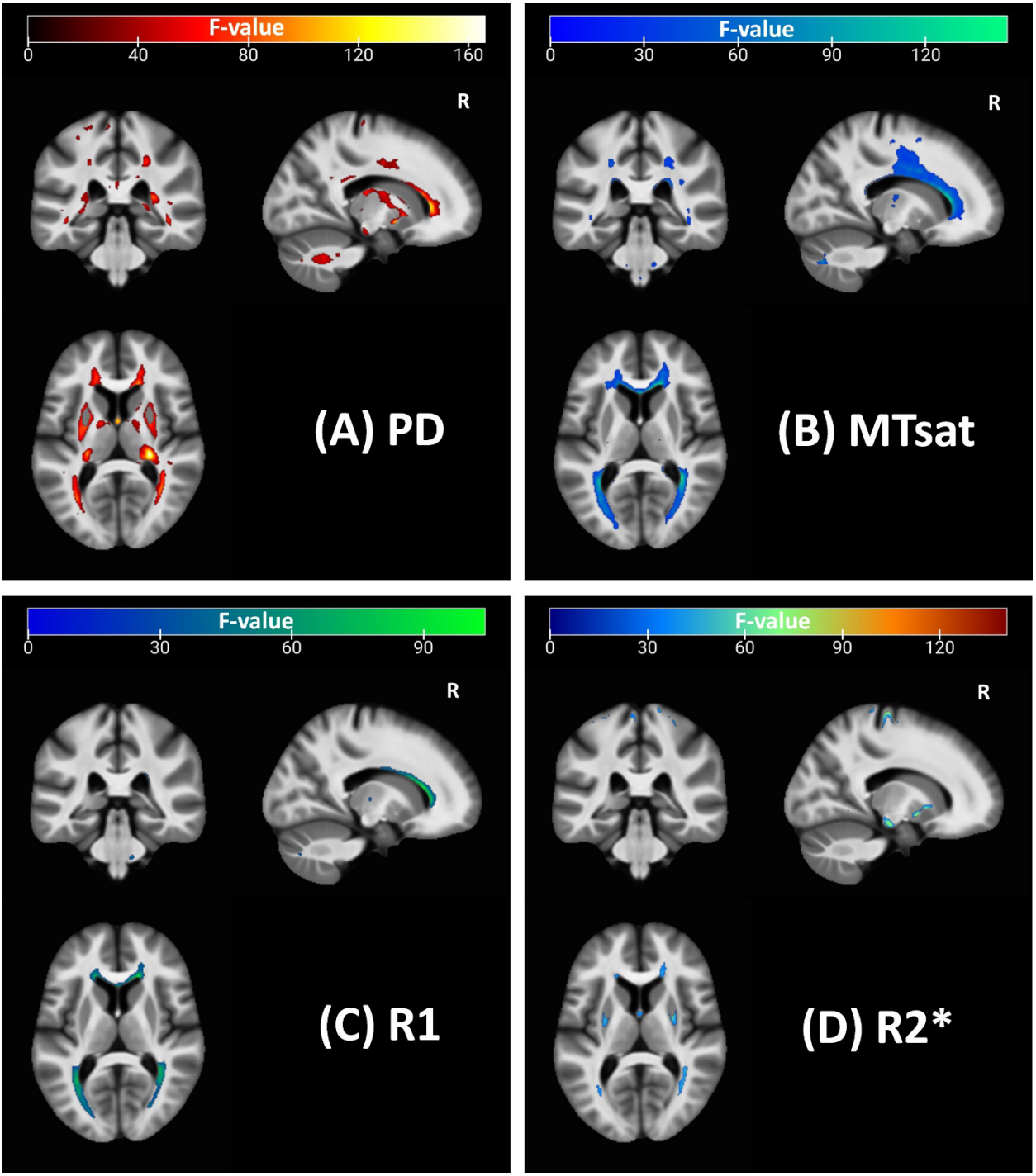

Figure 2. Statistical parametric maps of uGLMs in WM*; showing all the voxels with significant correlation with age, as detected by uGLMs for PD, MTsat, R1, and R2* maps. The F-tests were thresholded at p<0.0125 FWER corrected at voxel-level. The SPMs were overlayed on the mean MTsat map for the cohort in the MNI space. Abbreviation: GLM, general linear model, uGLM, univariate GLM, mGLM, multivariate GLM, WM, white matter, FWER, family-wise error, SPM, statistical parametric map.*

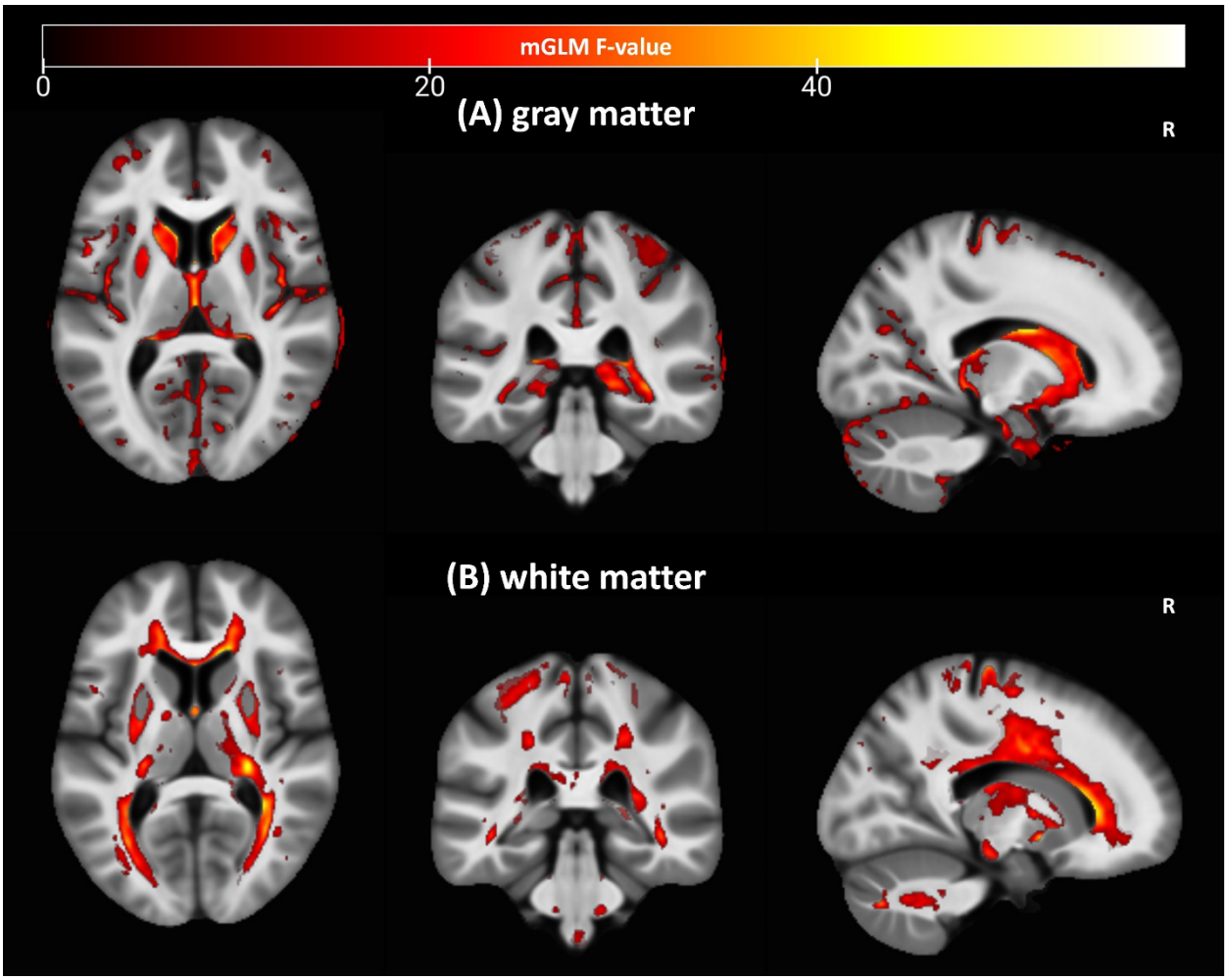

Figure 3. Statistical parametric maps of mGLMs in GM and WM*; showing all the voxels with significant correlation with age, as detected by the multivariate model. The F-tests were thresholded at p<0.05 FWER corrected at voxel-level. The SPMs were overlayed on the mean MTsat map for the cohort in the MNI space. Abbreviation: GLM, general linear model; mGLM, multivariate GLM; WM, white matter, FWER, family-wise error, SPM, statistical parametric map.*

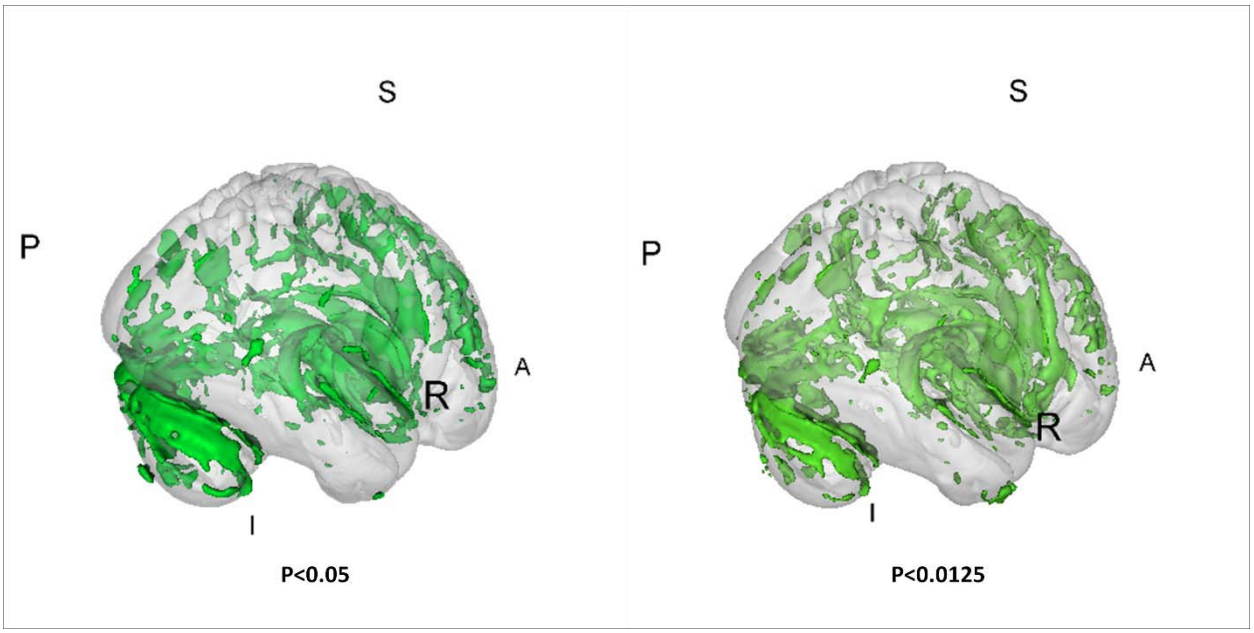

Figure 4. The union of all uGLM statistical parametric masks in GM*. On the left side, the F-tests for the uGLMs were thresholded at at p<0.05 FWER corrected at voxel-level. On the right side, the F-tests for the uGLMs were thresholded at P<0.0125 after correction for FWER at voxel-level. The masks were overlayed on the mean MTsat map for the cohort in the MNI space. Abbreviation: GLM, general linear model; uGLM, univariate GLM; GM, gray matter; FWER, family-wise error.*

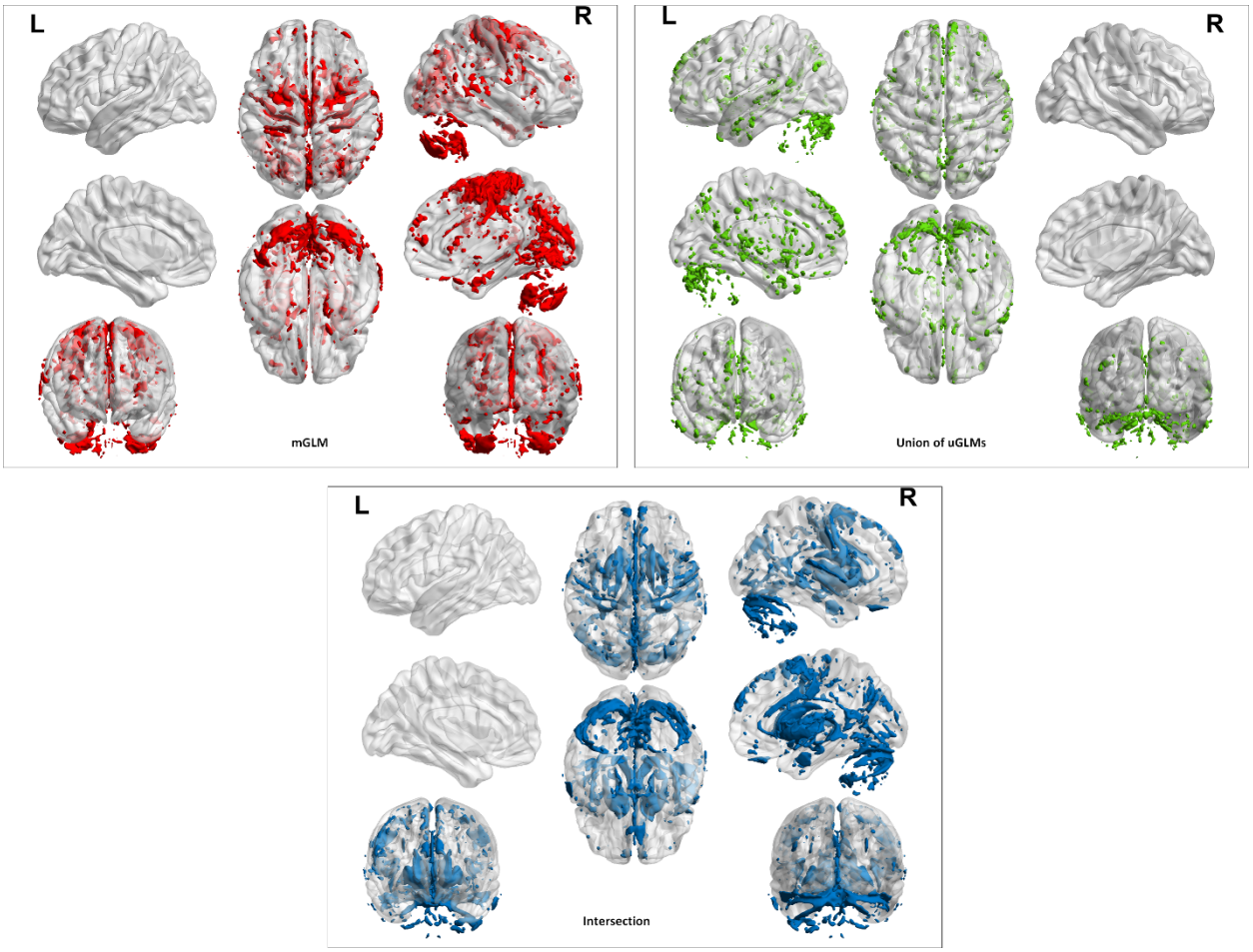

Figure 5. mGLM vs multiple uGLMs in GM*. The union of all uGLM statistical parametric masks (in green). And the mGLM results (in red). The F-tests for the uGLMs were thresholded at P<0.0125 after correction for FWER at voxel-level. The F-test for the mGLM was thresholded at P<0.05 FWER corrected at voxel-level. The masks were overlayed on MNI152 template image in BrainNet. Abbreviation: GLM, general linear model; uGLM, univariate GLM; mGLM, multivariate GLM; GM, gray matter; FWER, family-wise error.*

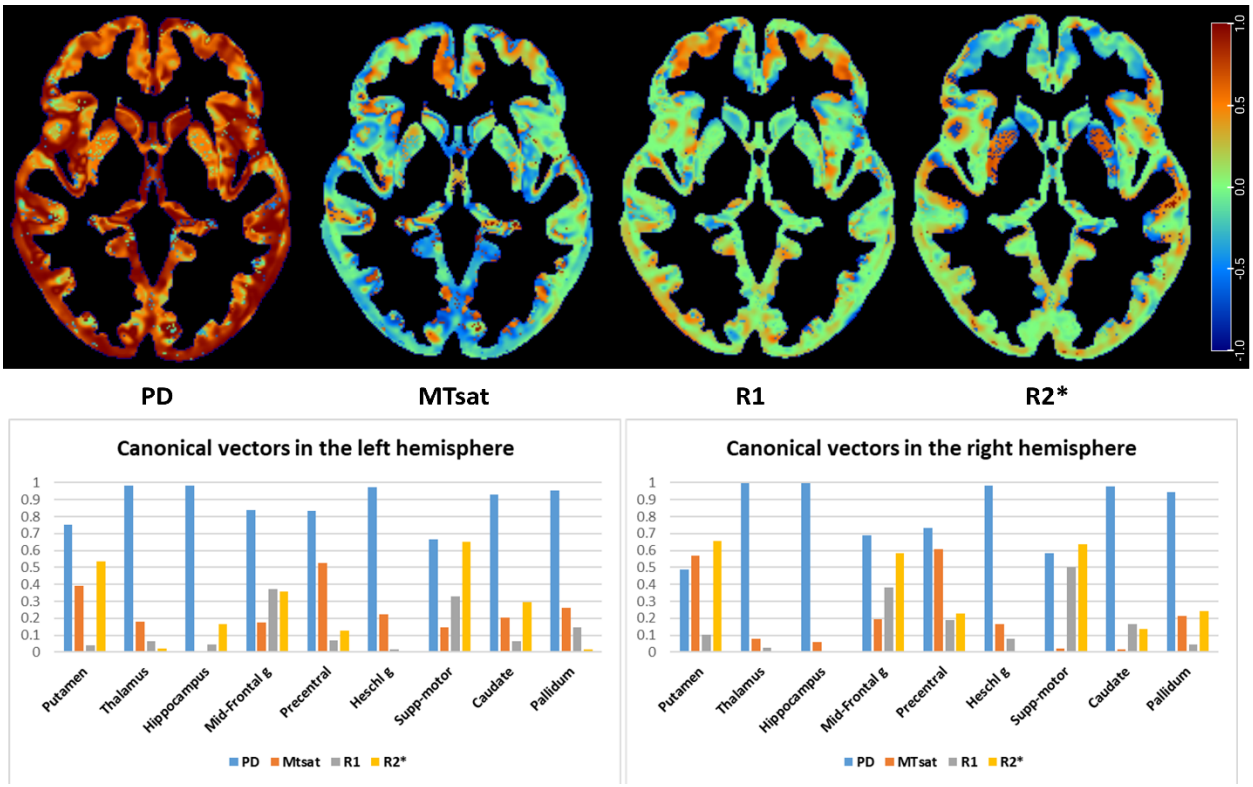

Figure 6. Canonical vectors for different modalities from the mGLM model*, representing the contribution of each modality in each voxel. The color bar shows arbitrary values. The vectors correspond to the peak voxels at the selected ROIs. Detailed vector sizes are reported in Table sup-1 of the supplementary data. Abbreviation: mGLM, multivariate general linear model; ROI, region of interest.*

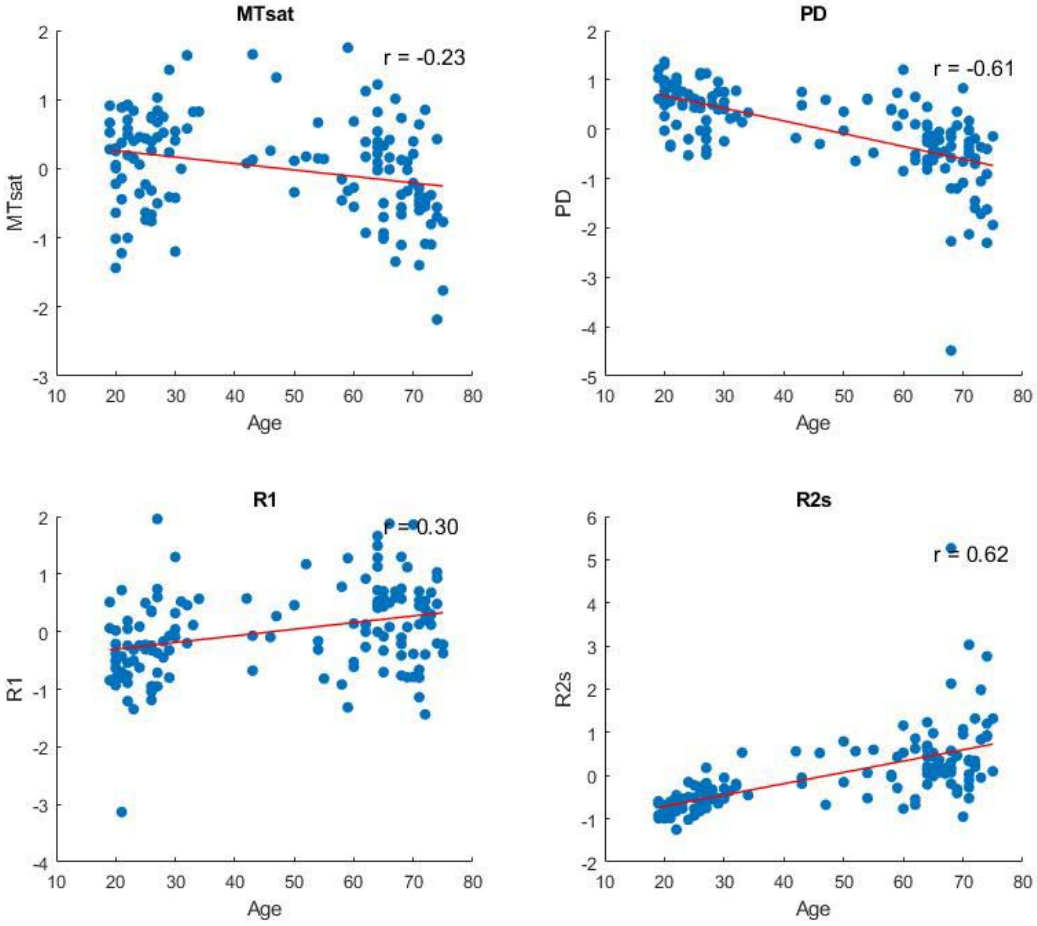

Figure 7. Median voxel values bilaterally in the Putamen. *The red lines depict the linear model fit. These data are shown for illustration purposes only and were not used for any additional analyses.*

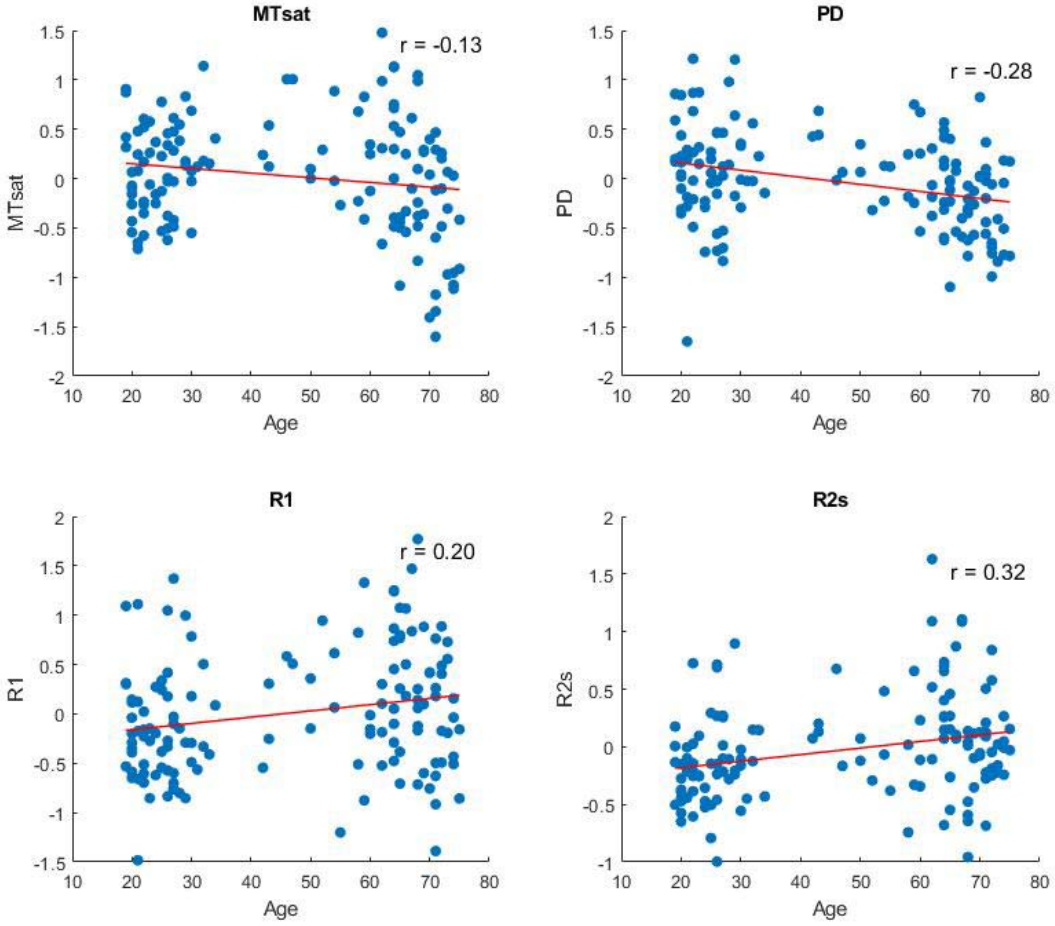

Figure 8. Median voxel values within the hippocampi*. The red lines depict the linear model fit. These data are shown for illustration purposes only and were not used for any additional analyses.*

Table 1. Summary statistics for significant voxels in uGLMs and mGLM. *"United" rows show the union of significant voxels in SPMs for all modalities. Univariate GLMs were thresholded at p<0.05 FWER corrected per tissue class (GM or WM). Abbreviation: GLM, general linear model; uGLM, univariate GLM; mGLM, multivariate GLM; GM, gray matter; WM, white matter.*

		Map name	#clusters	Cluster size	#voxels
GM	uGLMs	MTsat	284	1-42251	62334
		PD	271	1-7001	28563
		R1	181	1-1336	9078
		R2*	329	1-6416	44262
		United	666	1-82030	**115957**
	mGLM		564	1-130197	**154098**
WM	uGLMs	MTsat	58	1-67245	70285
		PD	78	1-7292	43051
		R1	36	1-11290	18301
		R2*	115	1-3789	18031
		United	191	1-84201	**105068**
	mGLM		188	1-82807	**102390**

Table 2. Summary statistics for significant voxels in uGLMs and mGLM. *"United" rows show the union of significant voxels in SPMs for all modalities. Univariate GLMs were thresholded at p<0.0125=.05/4 FWER corrected, to account for the multiplicity of maps tested (4) per tissue class (GM or WM). The mGLM was thresholded at p<0.05 FWER corrected. Abbreviation: GLM, general linear model, uGLM, univariate GLM, mGLM, multivariate GLM, SPM, statistical parametric maps, GM, gray matter, WM, white matter.*

		Map name	#clusters	Cluster size	#voxels
GM	uGLMs	MTsat	265	1-16445	50041
		PD	212	1-6671	22168
		R1	142	1-670	6276
		R2*	256	1-5919	31993
		United	570	1-54926	**90323**
	mGLM		564	1-130197	**154098**
WM	uGLMs	MTsat	45	1-52838	35281
		PD	73	6378	54894
		R1	27	1-8640	14344
		R2*	101	1-3223	13518
		United	163	1-56506	**83187**
	mGLM		188	1-82807	**102390**

Table 3. Pearson Partial Correlations *on the median voxel values within different regions of interest.*

s	Pearson's r	p-value	Effect size (Fisher's z)	SE Effect size		Pearson's r	p-value	Effect size (Fisher's z)	SE Effect size
Caudate					**Pallidum**				
MTsat	-0.437***	< .001	-0.469	0.087	MTsat	-0.099	0.253	-0.099	0.087
PD	-0.635***	< .001	-0.749	0.087	PD	-0.696***	< .001	-0.860	0.087
R1	0.092	0.289	0.092	0.087	R1	0.440***	< .001	0.472	0.087
R2s	0.476***	< .001	0.517	0.087	R2s	0.665***	< .001	0.802	0.087
Cerebellum					**Precentral Gyrus**				
MTsat	-0.550***	< .001	-0.619	0.087	MTsat	-0.344***	< .001	-0.358	0.087
PD	-0.265**	0.002	-0.272	0.087	PD	-0.440***	< .001	-0.472	0.087
R1	-0.111	0.198	-0.112	0.087	R1	-0.016	0.852	-0.016	0.087
R2s	0.385***	< .001	0.406	0.087	R2s	0.496***	< .001	0.545	0.087
Heschl Gyrus					**Putamen**				
MTsat	-0.511***	< .001	-0.564	0.087	MTsat	-0.233**	0.007	-0.237	0.087
PD	-0.180*	0.037	-0.182	0.087	PD	-0.610***	< .001	-0.709	0.087
R1	-0.211*	0.014	-0.214	0.087	R1	0.298***	< .001	0.307	0.087
R2s	0.215*	0.012	0.218	0.087	R2s	0.616***	< .001	0.719	0.087
Middle Frontal Gyrus					**Superior motor cortex**				
MTsat	-0.131	0.129	-0.132	0.087	MTsat	-0.128	0.139	-0.129	0.087
PD	-0.448***	< .001	-0.483	0.087	PD	-0.446***	< .001	-0.480	0.087
R1	0.069	0.423	0.070	0.087	R1	0.051	0.560	0.051	0.087
R2s	0.437***	< .001	0.468	0.087	R2s	0.590***	< .001	0.677	0.087
Hippocampus					**Thalamus**				
MTsat	-0.131	0.130	-0.132	0.087	MTsat	-0.562***	< .001	-0.636	0.087
PD	-0.282***	< .001	-0.289	0.087	PD	-0.236**	0.006	-0.240	0.087
R1	0.200*	0.020	0.203	0.087	R1	-0.353***	< .001	-0.369	0.087
R2s	0.316***	< .001	0.327	0.087	R2s	-0.197*	0.022	-0.199	0.087

Note. Conditioned on variables: Gender, TIV, TRIO. * p < .05, ** p < .01, *** p < .001

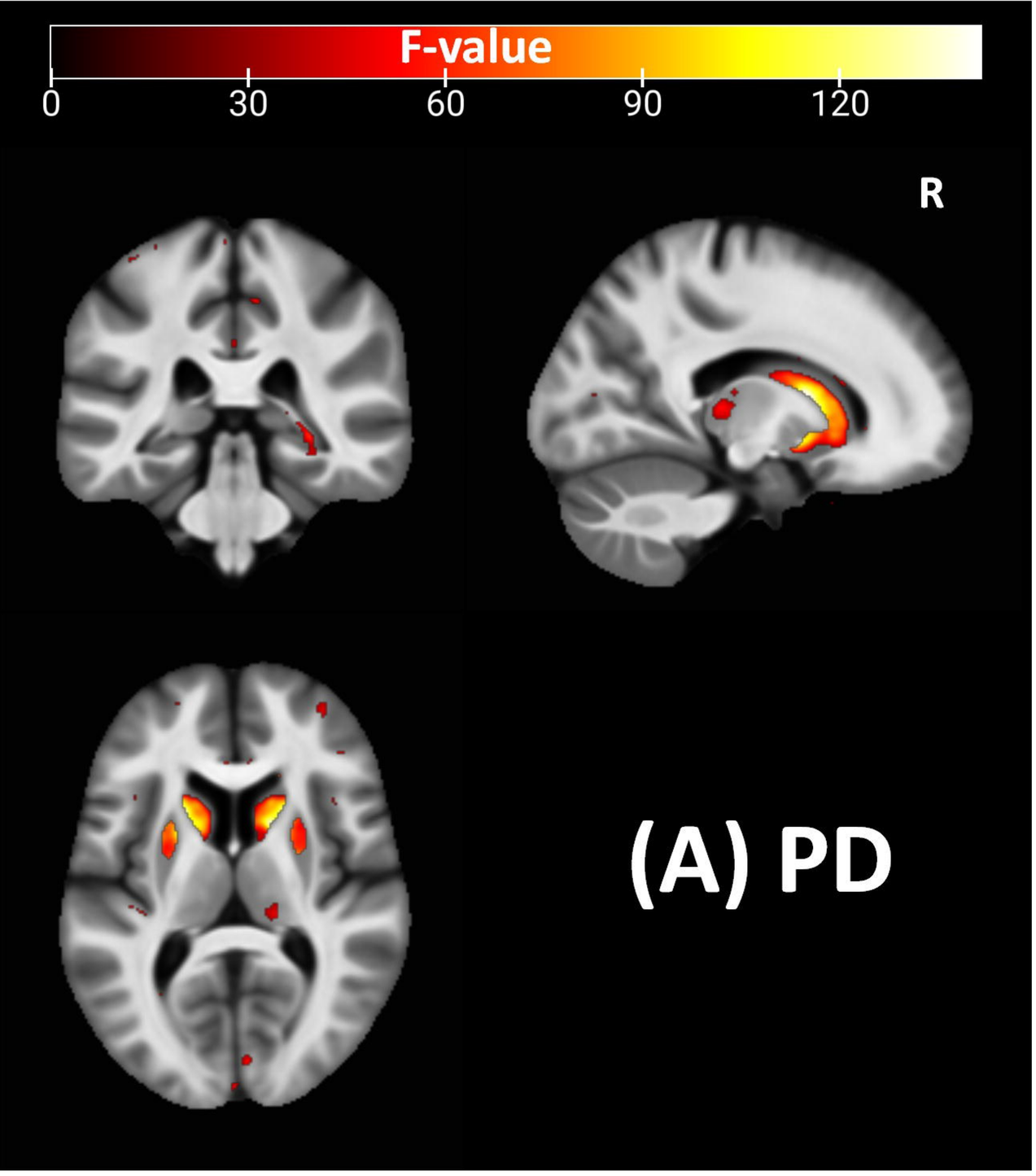

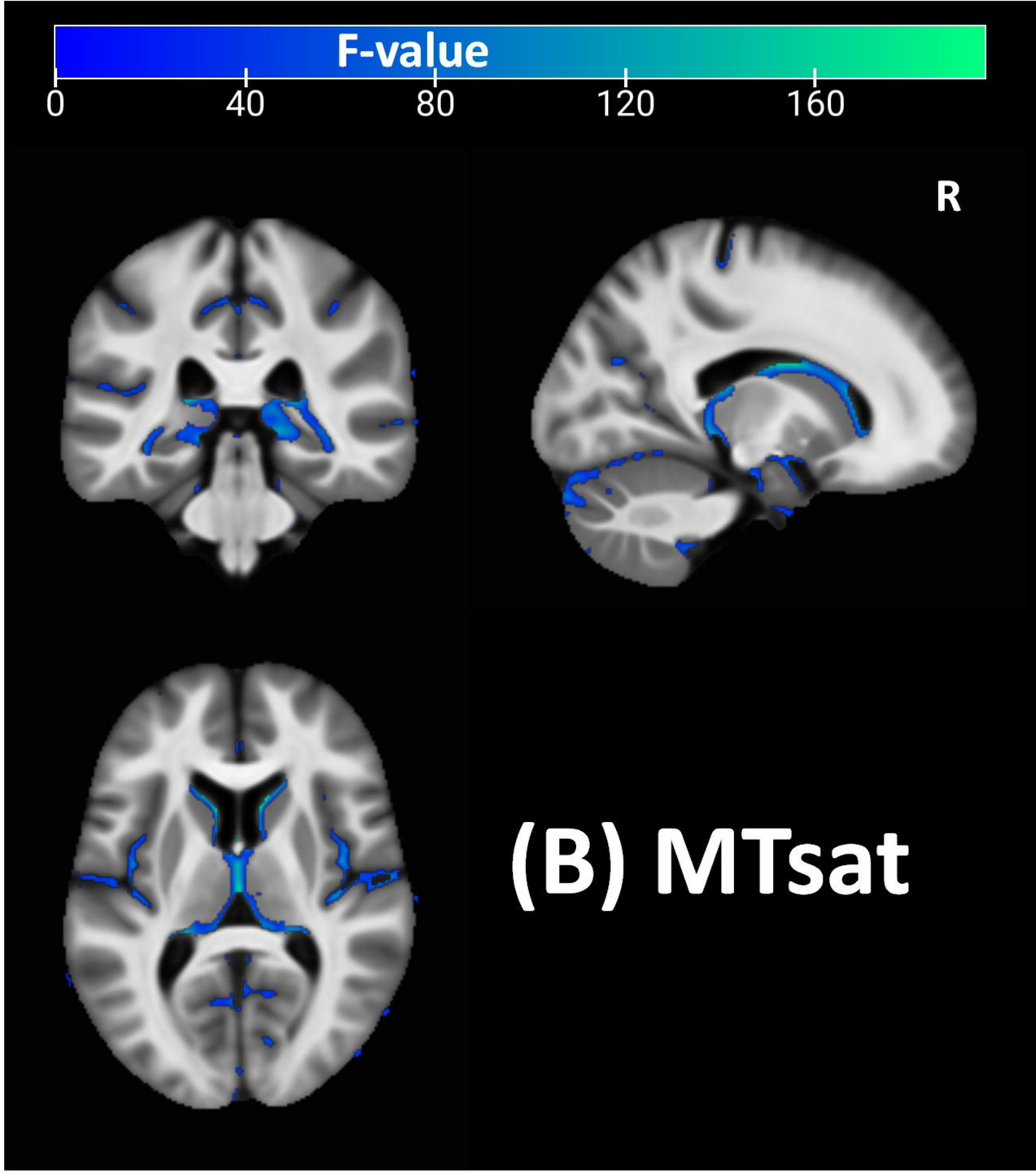

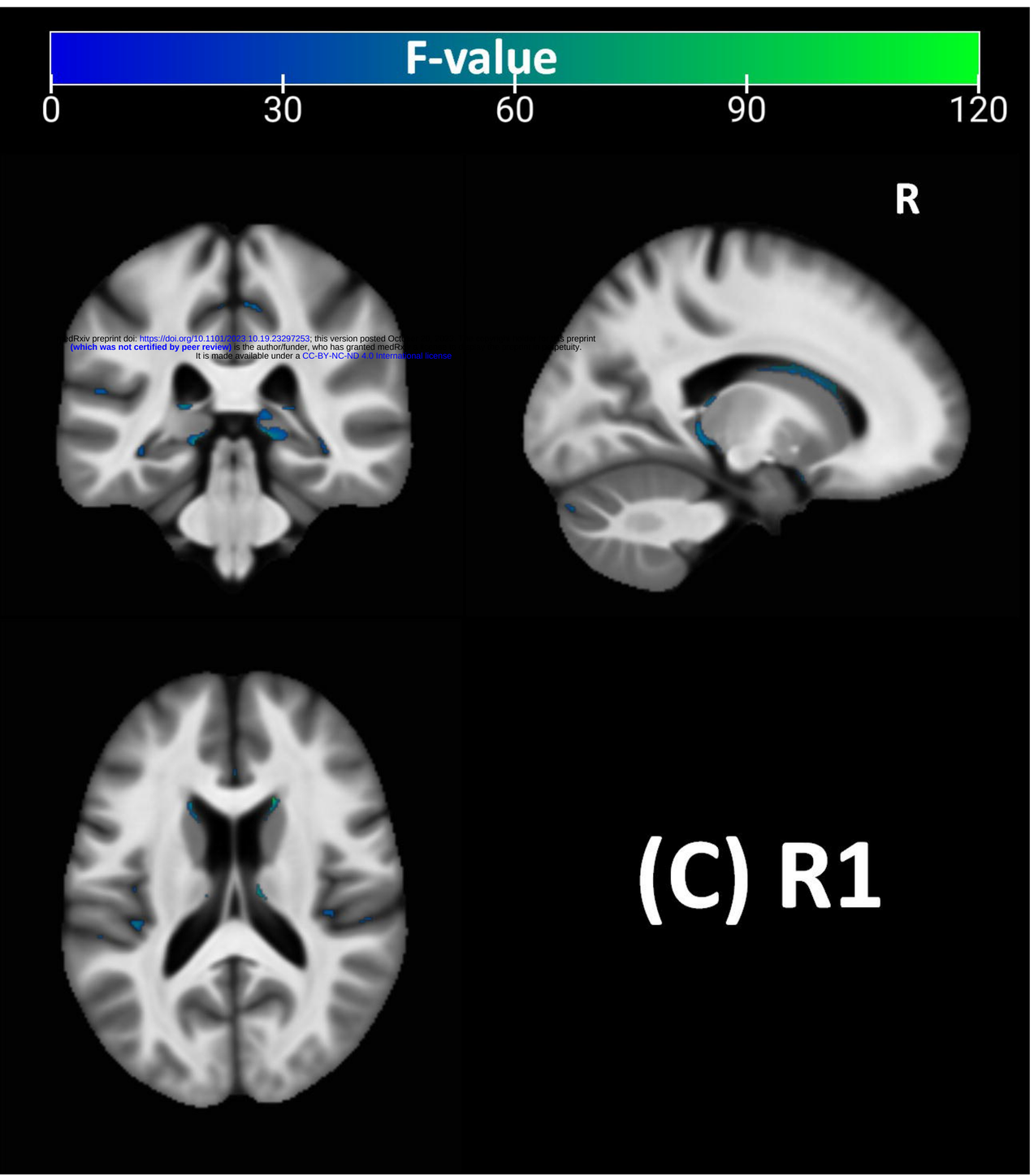

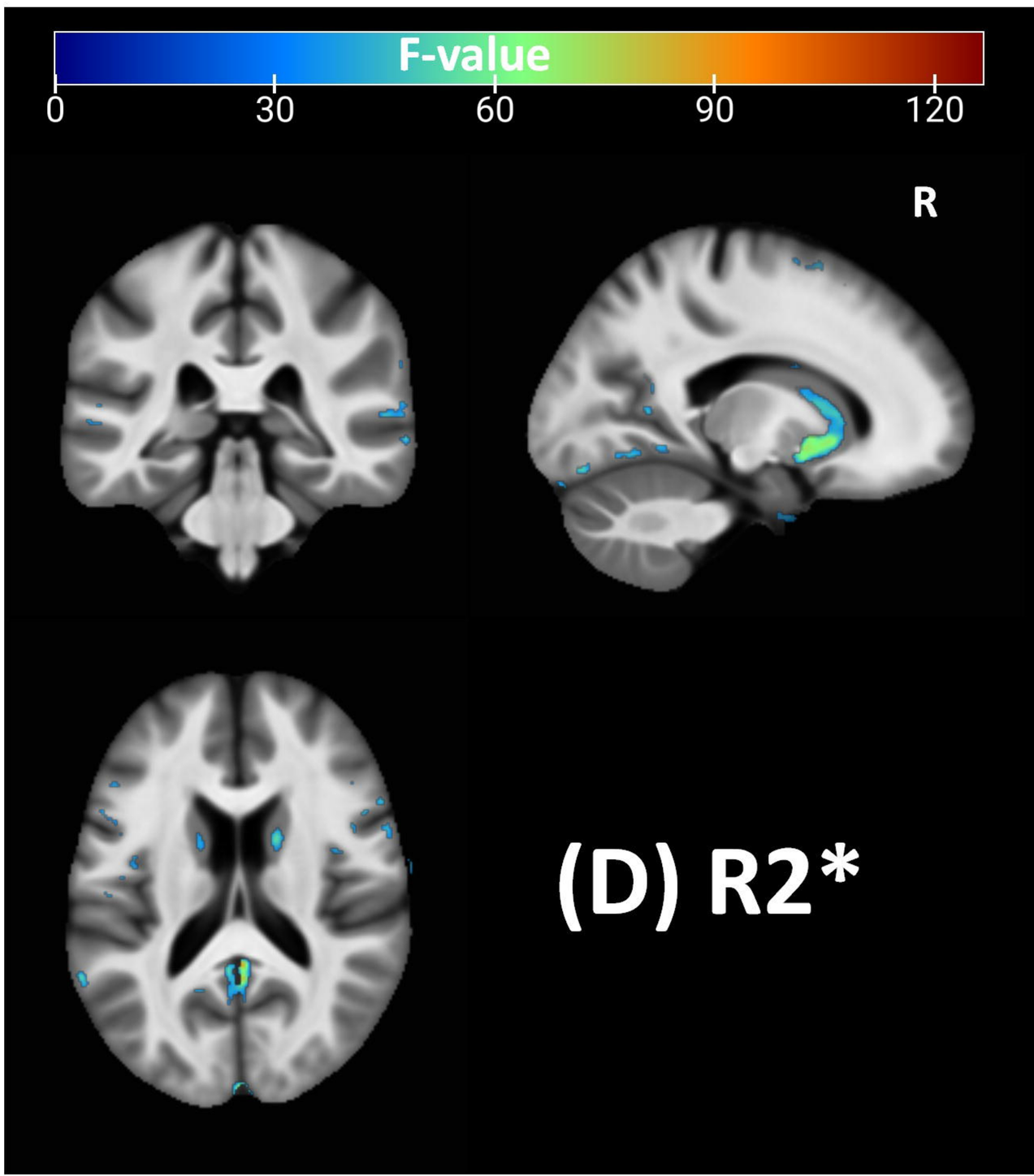

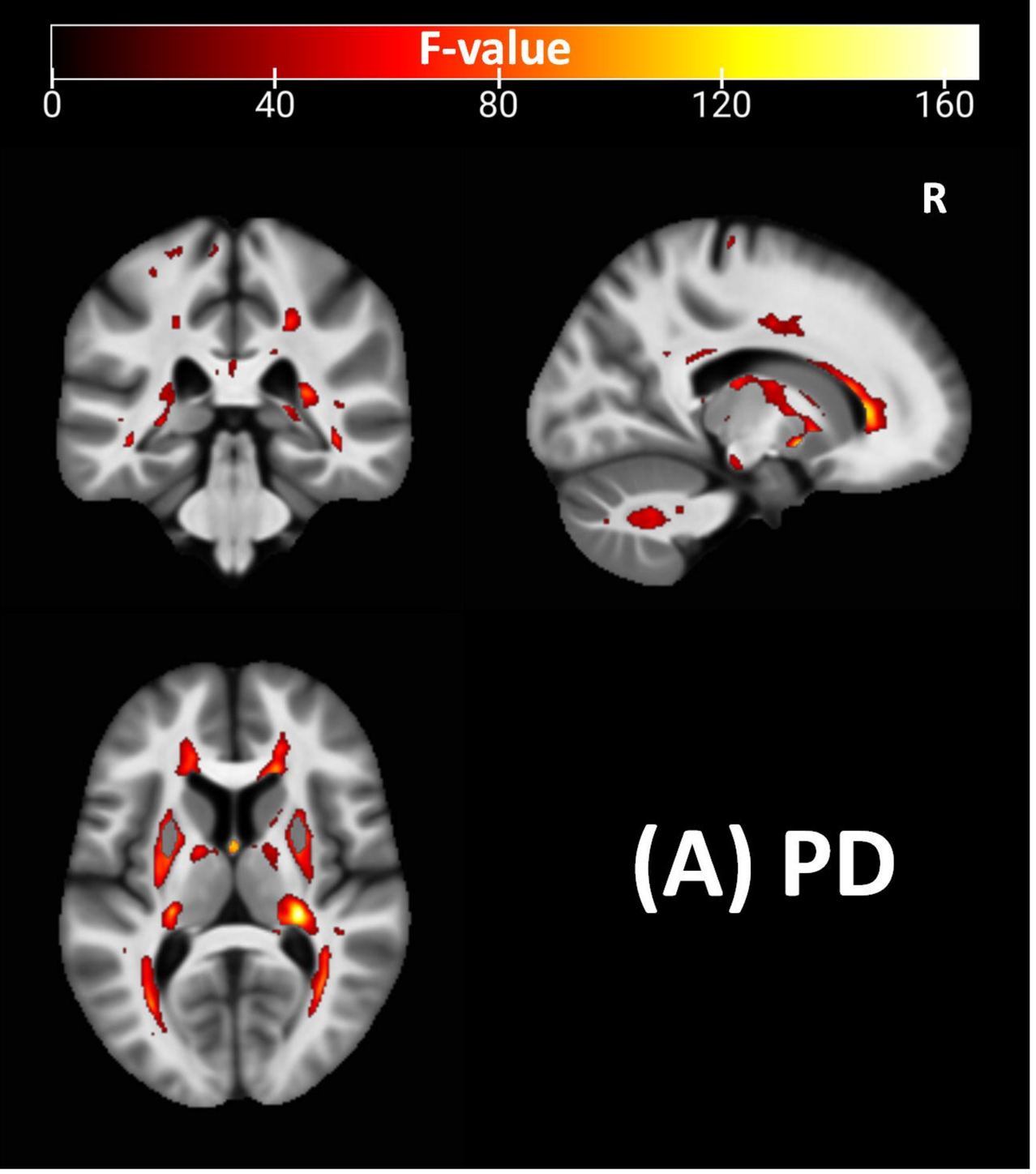

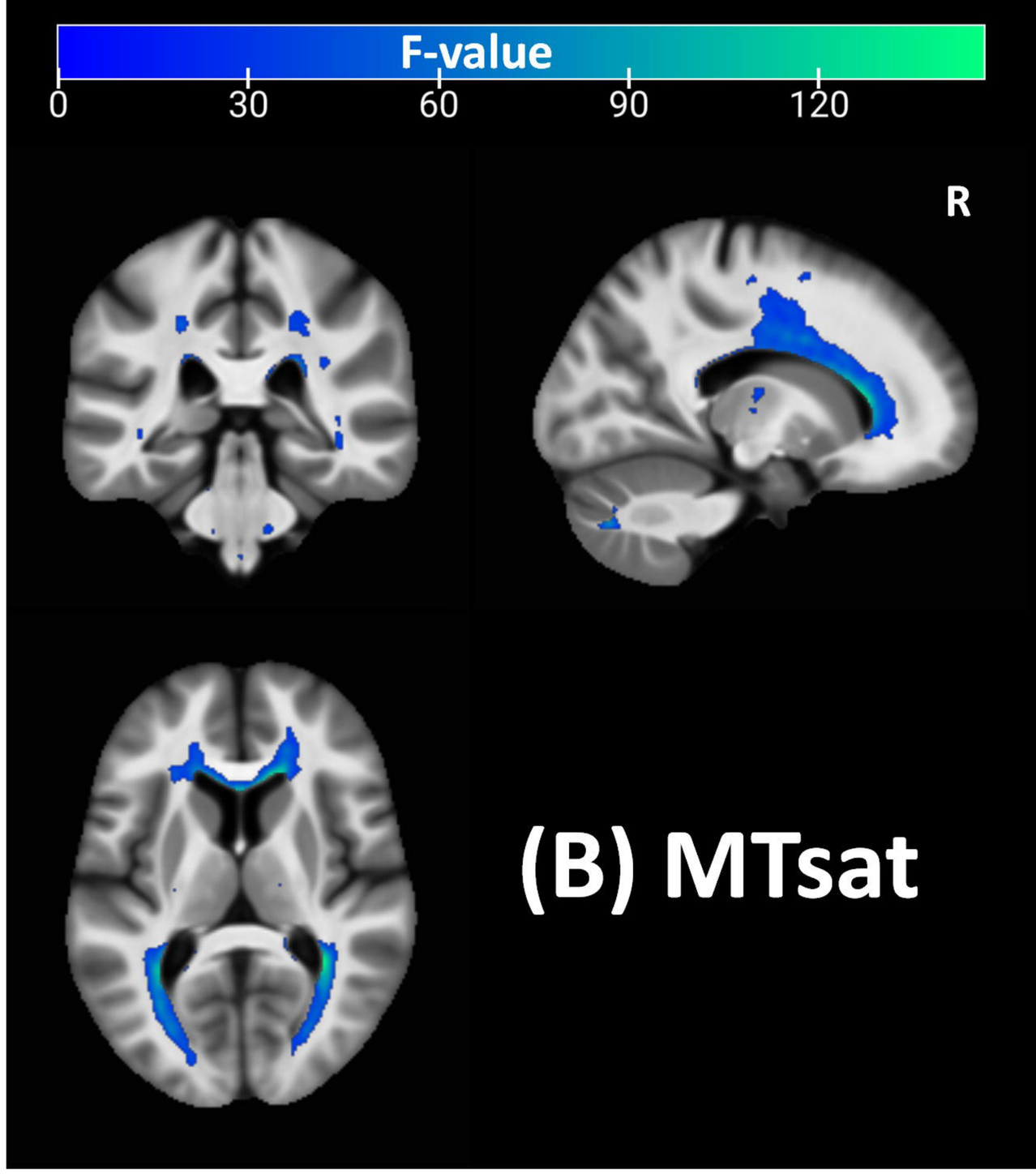

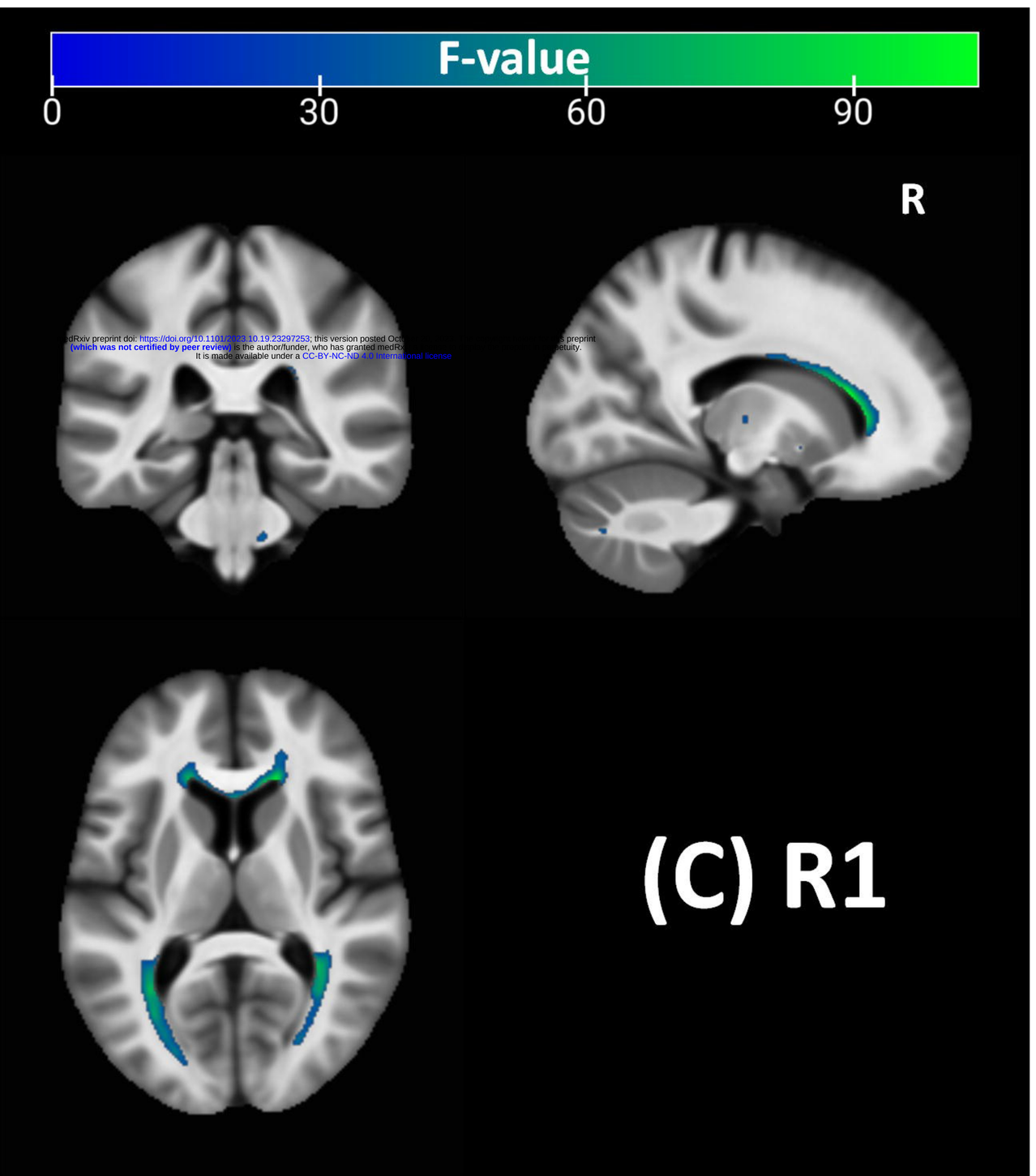

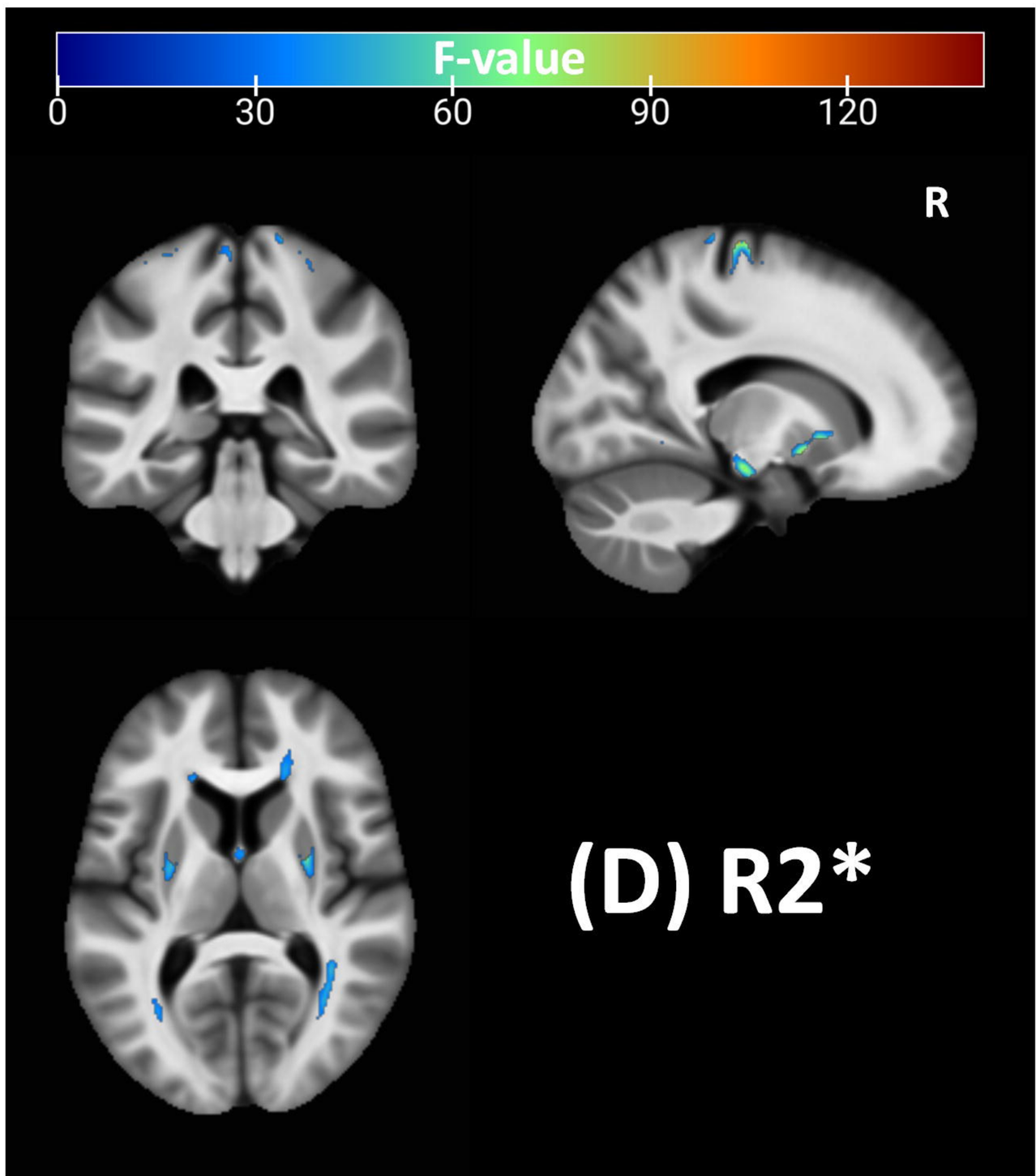

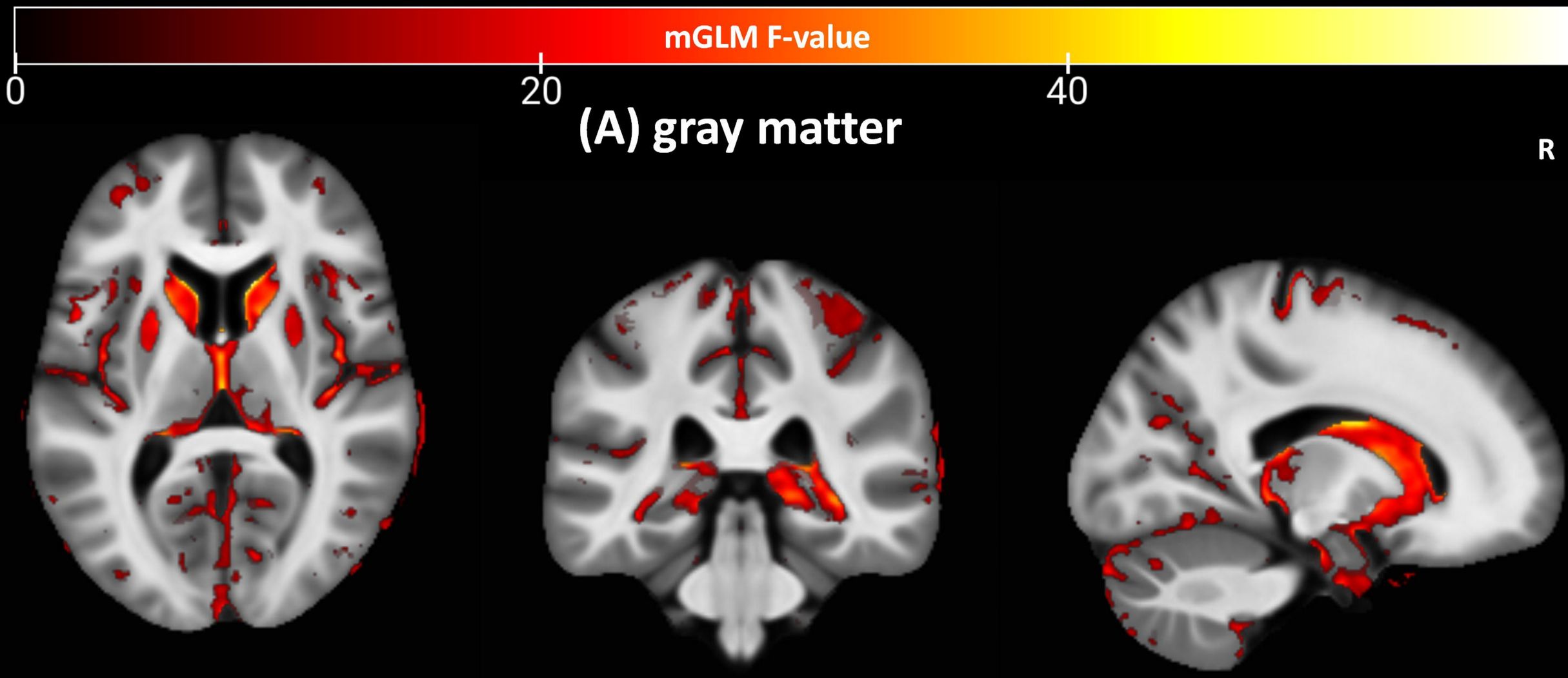

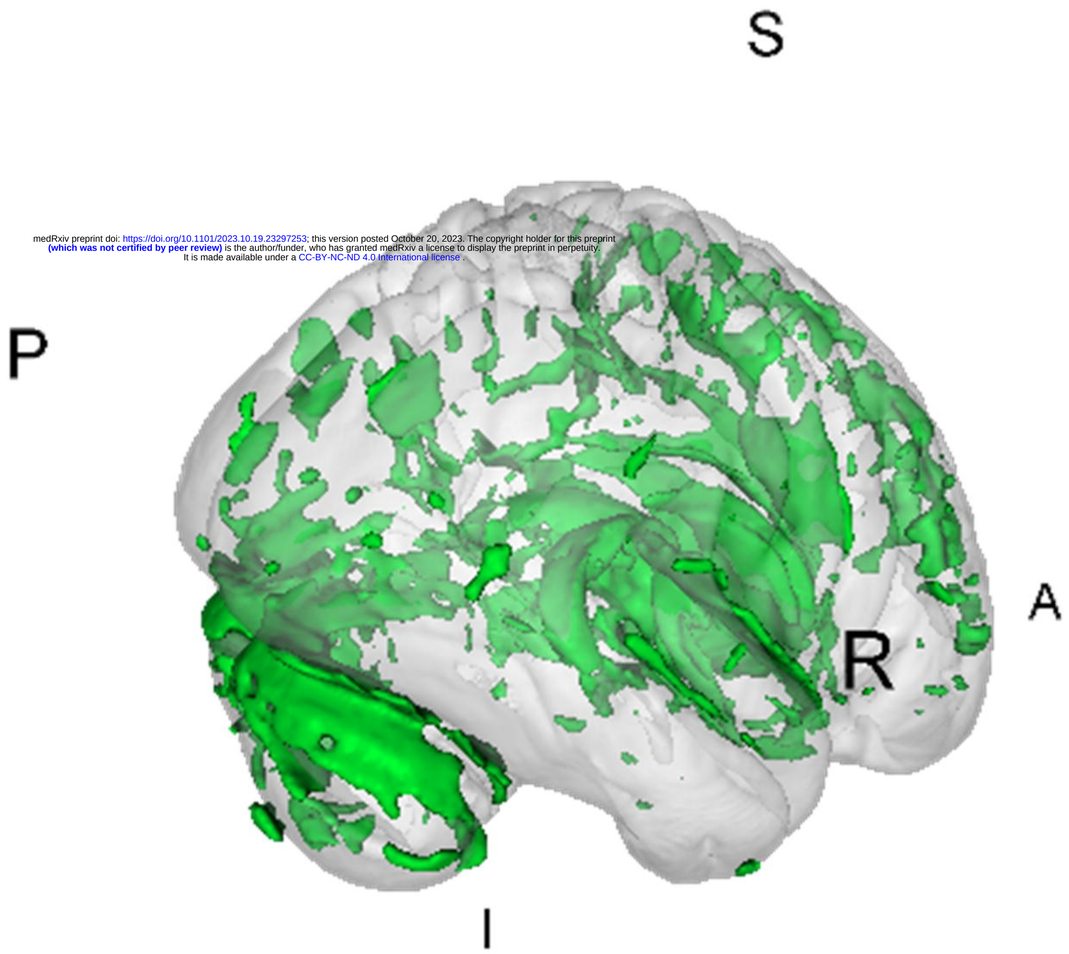

P<0.05

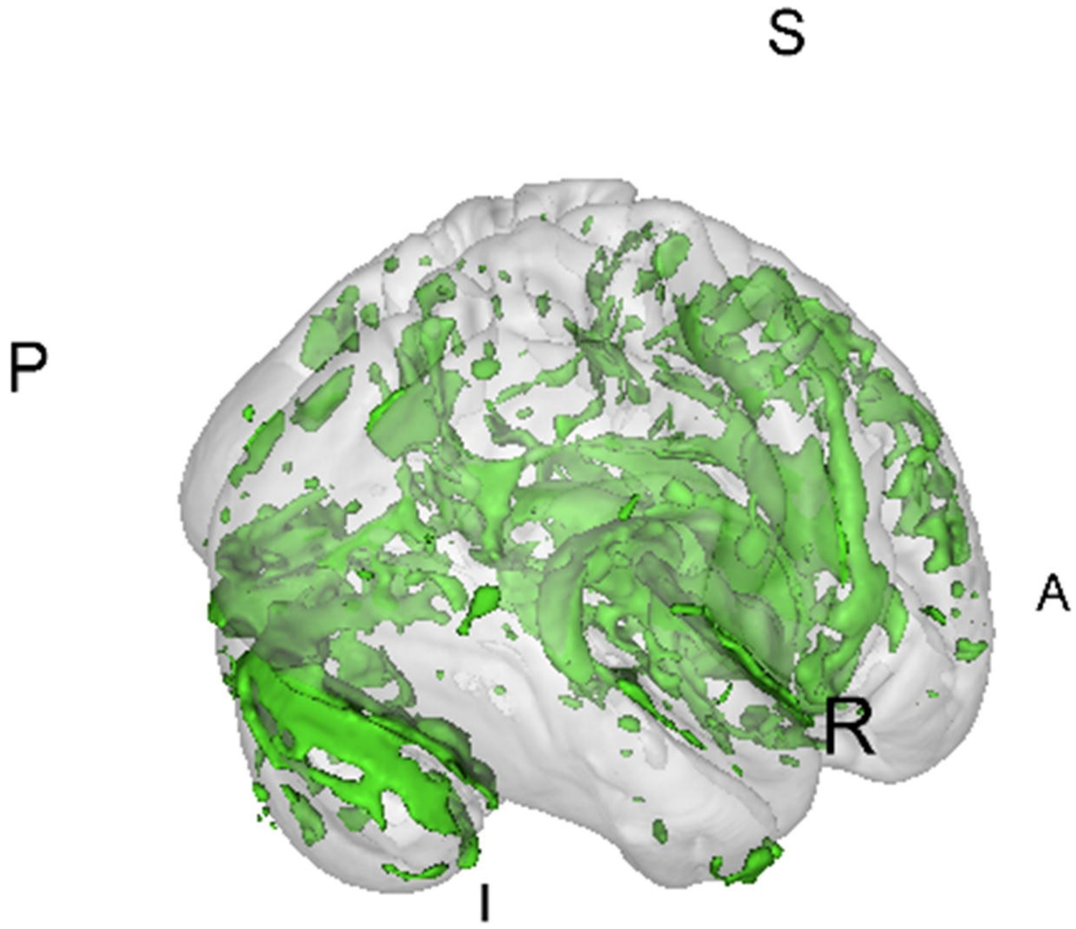

P<0.0125

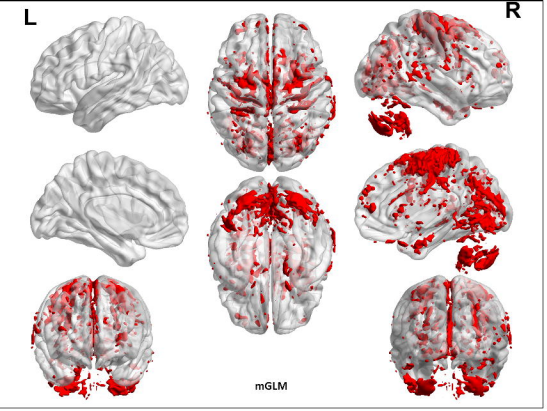
L
R
mGLM

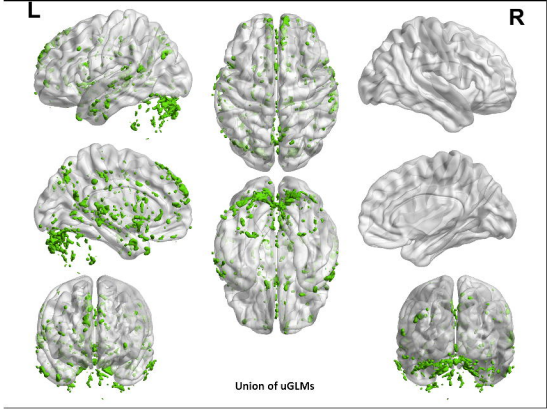
L
R
Union of uGLMs

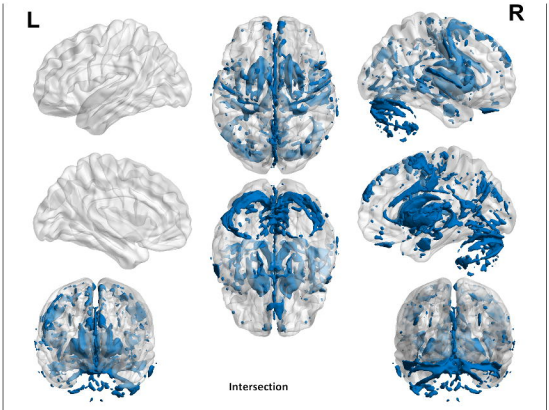
L
R
Intersection

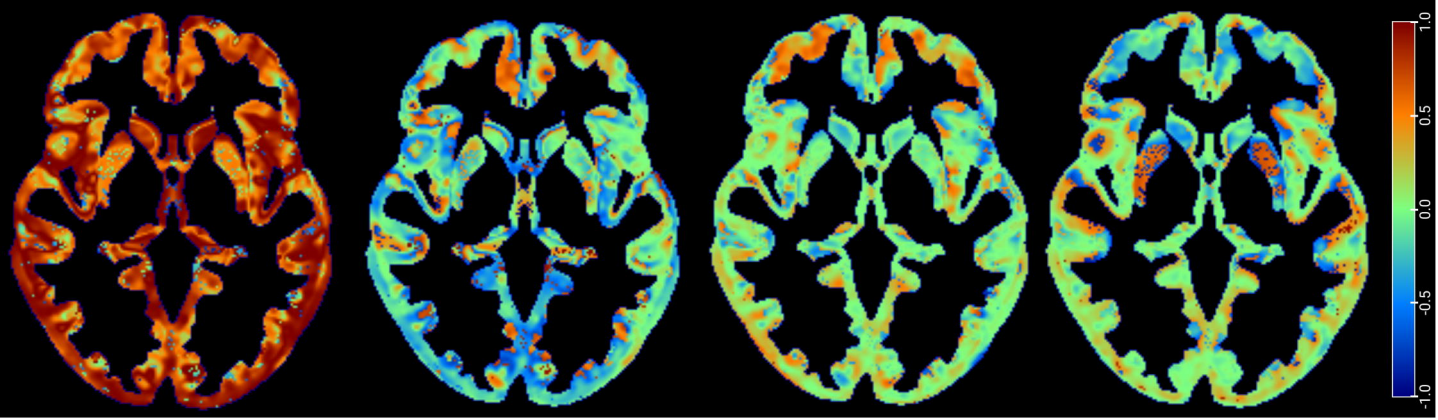

PD MTsat R1 R2*

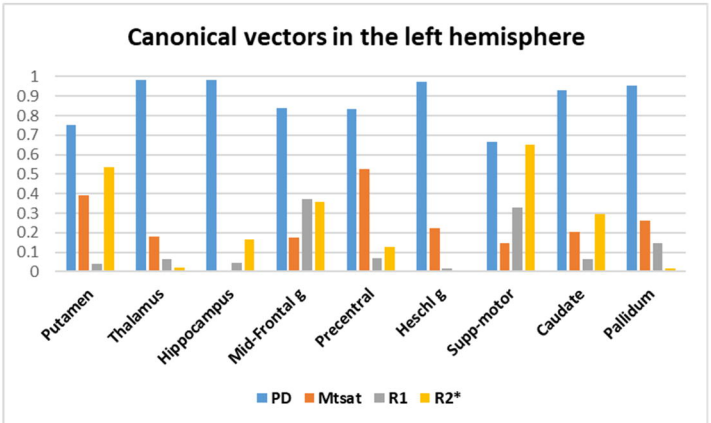

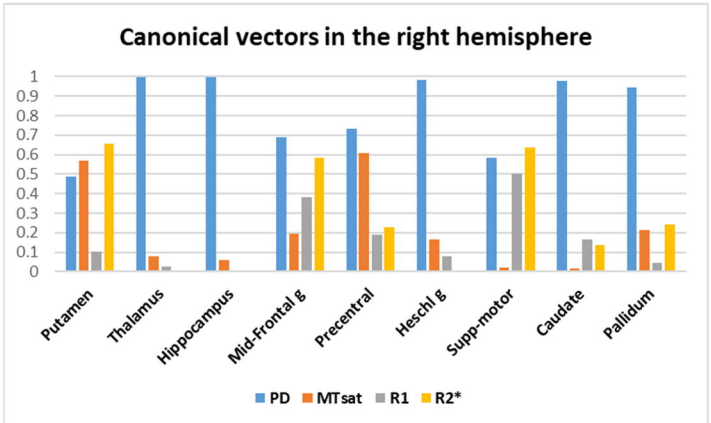

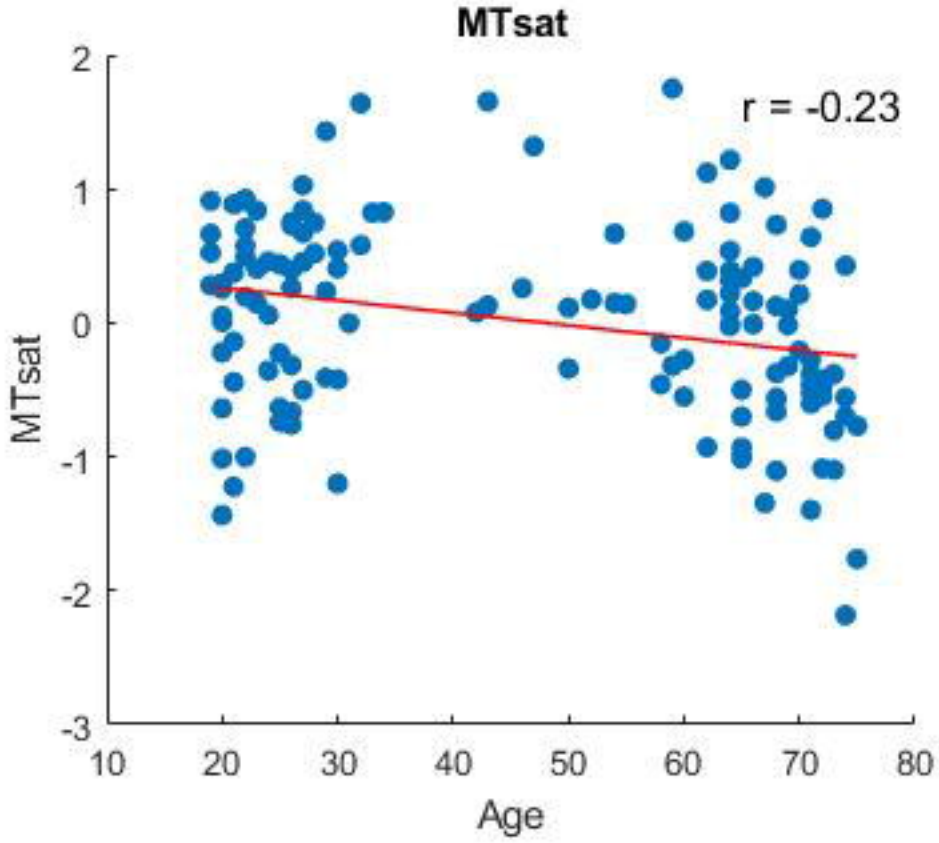
MTsat
r = -0.23
MTsat
Age
2
1
0
-1
-2
-3
10
20
30
40
50
60
70
80

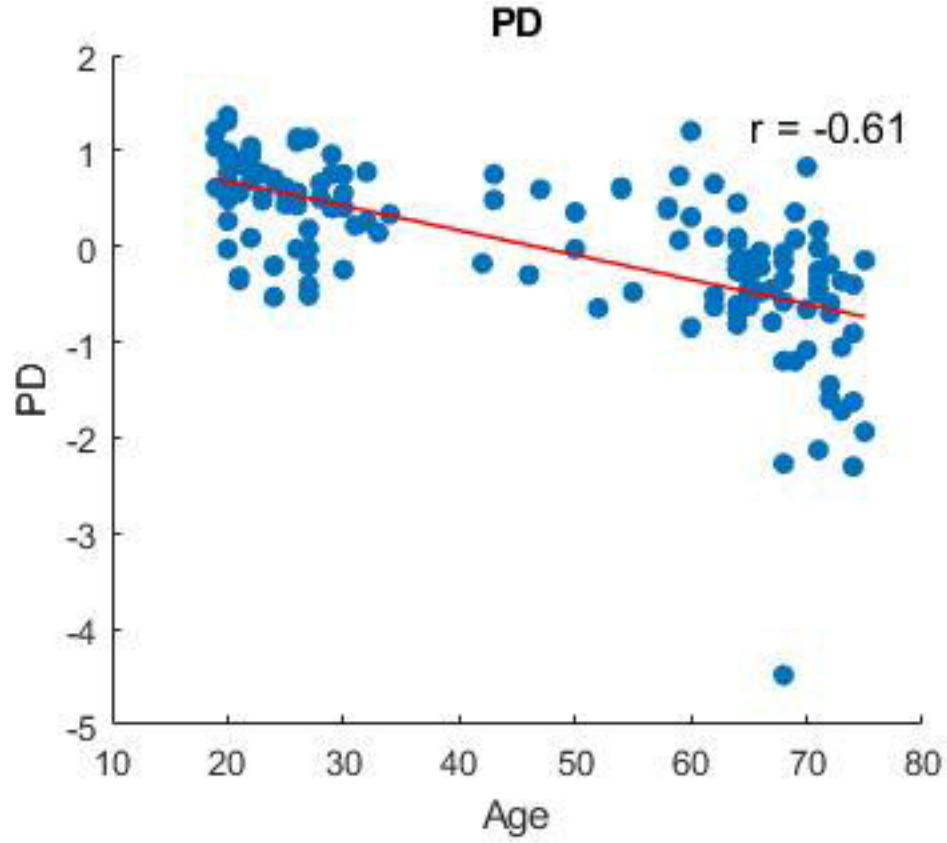
PD
r = -0.61
PD
Age
2
1
0
-1
-2
-3
-4
-5
10
20
30
40
50
60
70
80

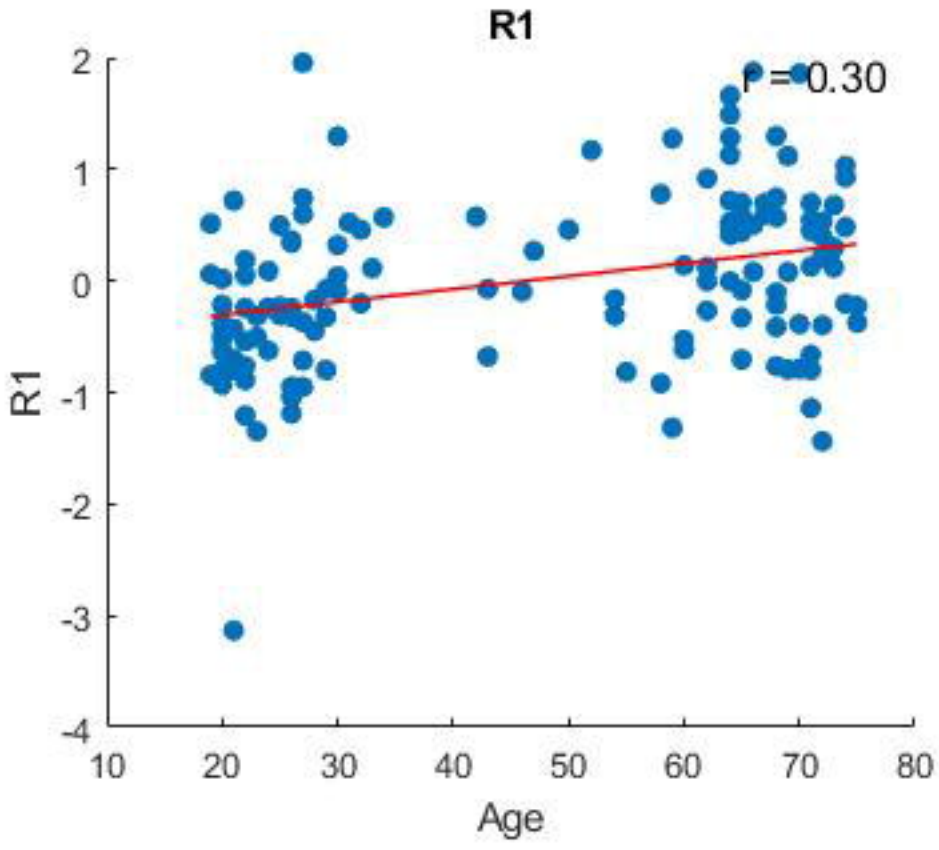
R1
r = 0.30
R1
Age
2
1
0
-1
-2
-3
-4
10
20
30
40
50
60
70
80

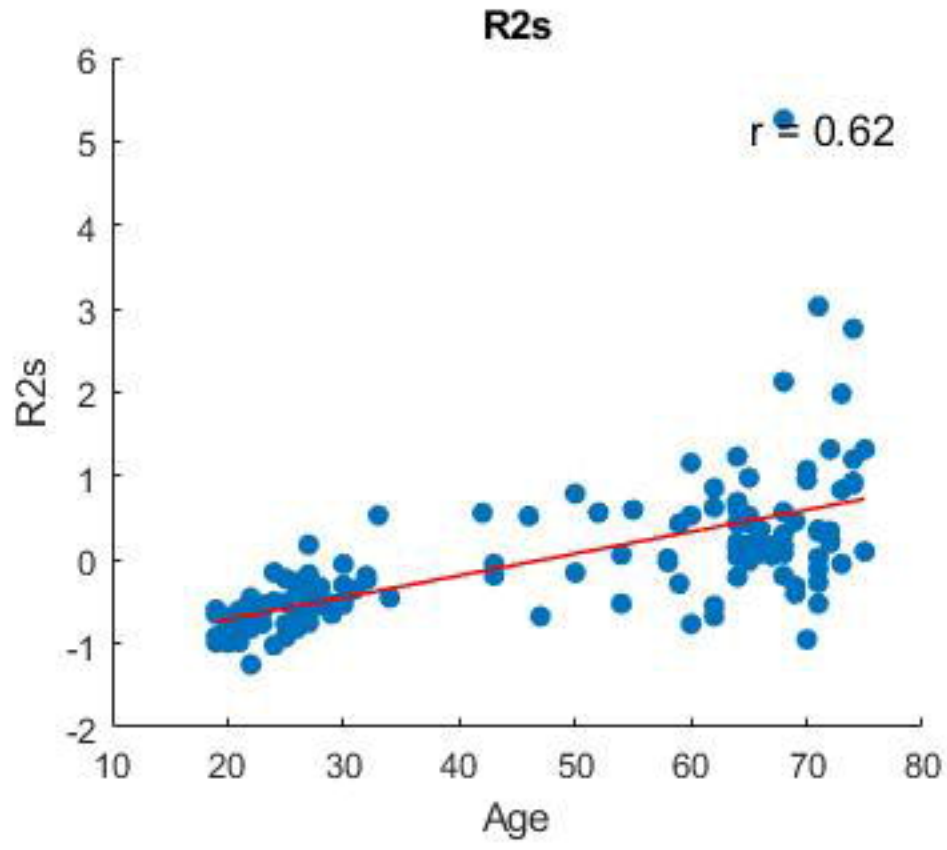
R2s
r = 0.62
R2s
Age
6
5
4
3
2
1
0
-1
-2
10
20
30
40
50
60
70
80

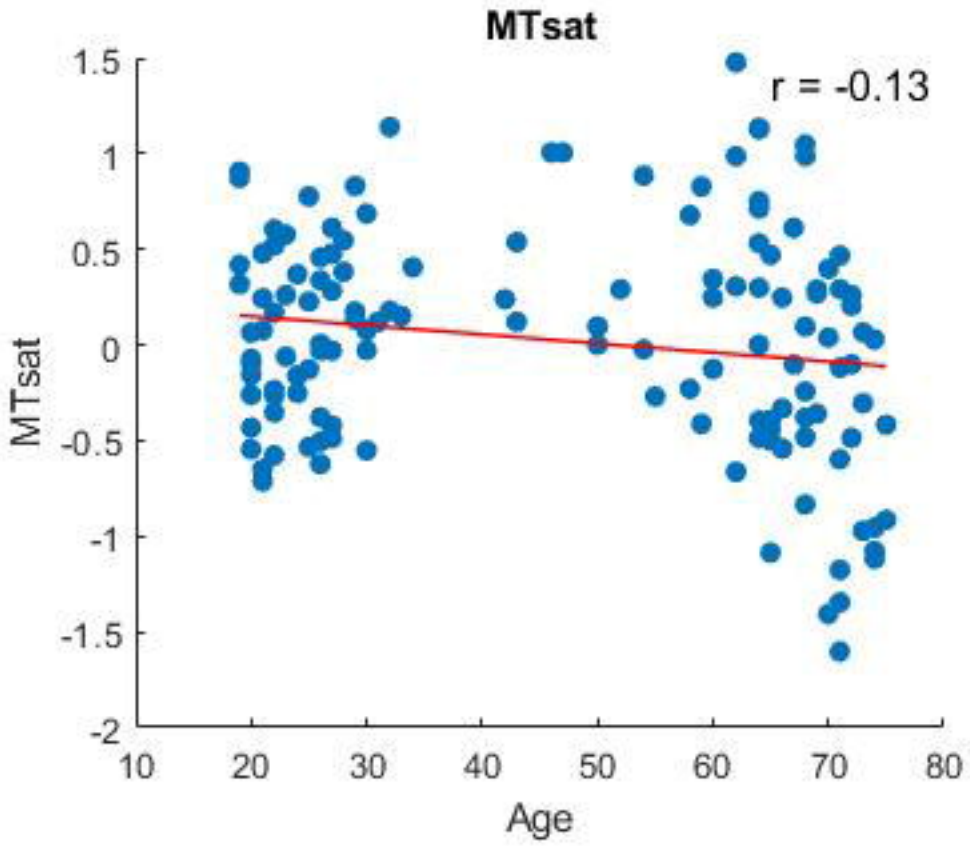
MTsat
r = -0.13
MTsat
Age
1.5
1
0.5
0
-0.5
-1
-1.5
-2
10
20
30
40
50
60
70
80

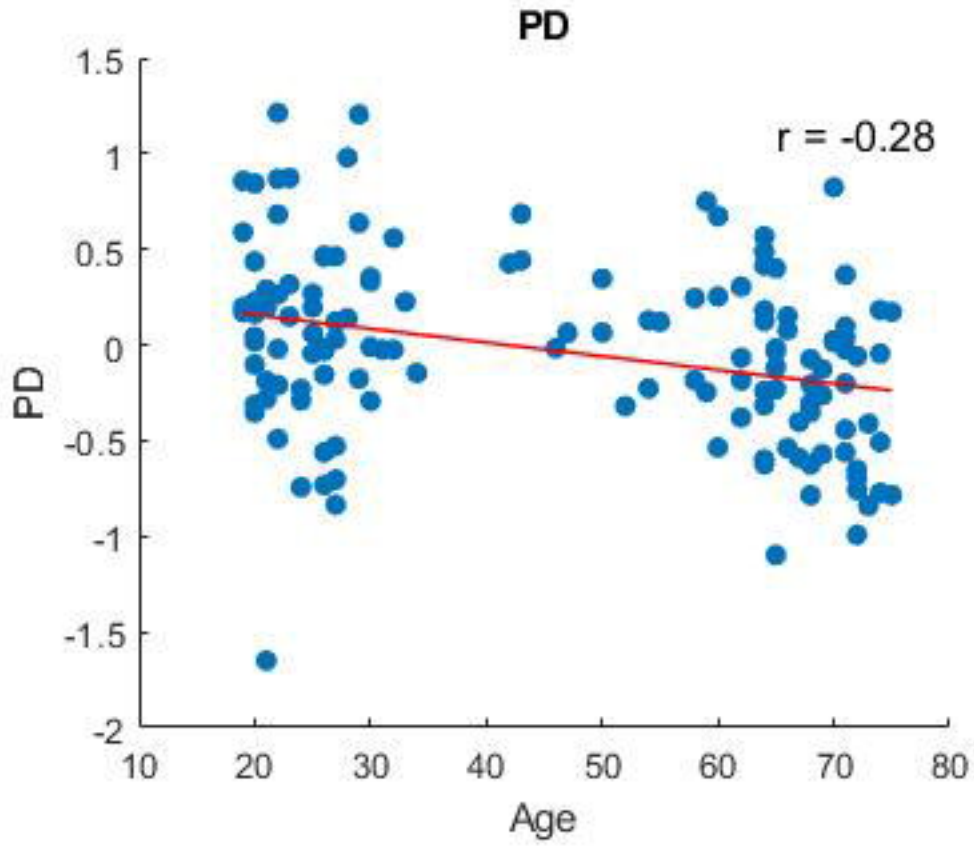
PD
r = -0.28
PD
Age
1.5
1
0.5
0
-0.5
-1
-1.5
-2
10
20
30
40
50
60
70
80

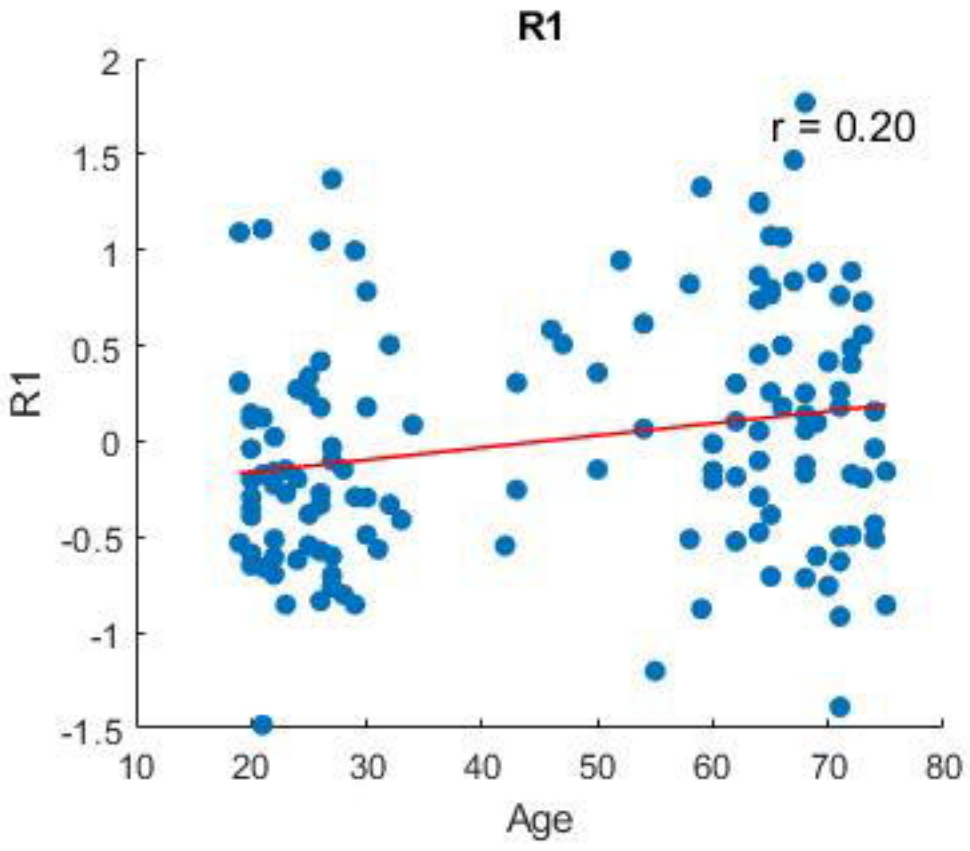
R1
r = 0.20
R1
Age
2
1.5
1
0.5
0
-0.5
-1
-1.5
10
20
30
40
50
60
70
80

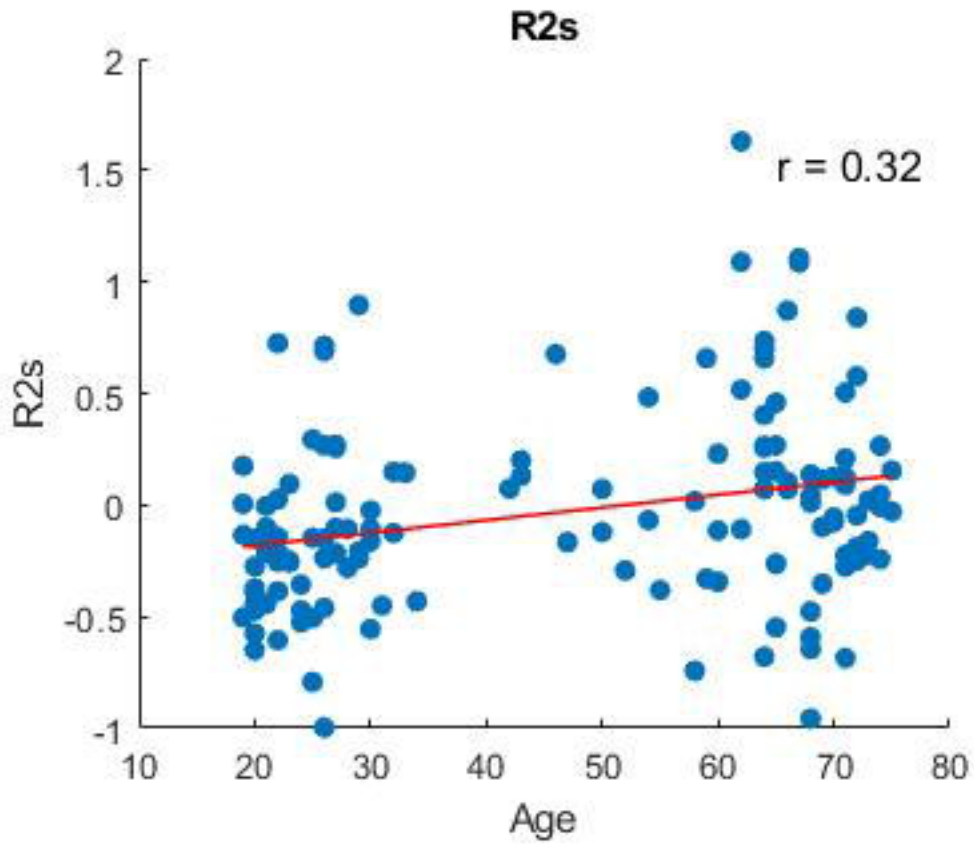
R2s
r = 0.32
R2s
Age
2
1.5
1
0.5
0
-0.5
-1
10
20
30
40
50
60
70
80